Mon. Not. R. Astron. Soc. **000**, 1–21 (2008) Printed 11 August 2008 (MN LaTeX style file v2.2)

arXiv:0808.0881v2 [astro-ph] 11 Aug 2008

Signatures of clumpy dark matter in the global 21 cm background signal

D. T. Cumberbatch[1]⋆ M. Lattanzi[1,2]† and J. Silk[1]‡
[1] *Oxford Astrophysics, Denys Wilkinson Building, Keble Road, Oxford, OX1 3RH, U.K.*
[2] *Istituto Nazionale di Fisica Nucleare, Via Enrico Fermi, 40 - 00044 Frascati, Rome, Italy.*

11 August 2008

ABSTRACT
We examine the extent to which the self-annihilation of supersymmetric neutralino dark matter, as well as light dark matter, influences the rate of heating, ionisation and Lyman-α pumping of interstellar hydrogen and helium and the extent to which this is manifested in the 21cm background signal. Unlike previous studies we fully consider the enhancements to the annihilation rate from dark matter halos and substructures within them. We find that the influence of such structures results in significant changes in the brightness temperature. The effect on the global signature at redshifts within the range probed LOFAR (i.e. $z < 12$) is on the edge of its sensitivity in the case of neutralino dark matter, and very likely to be detected for annihilating light dark matter.

Key words: Cosmology: dark matter, Intergalactic Medium

1 INTRODUCTION

The standard cosmological model, motivated by measurements of temperature anisotropies in the Cosmic Microwave Background (CMB) (Spergel et al. 2003, 2007; Komatsu et al. 2008; Dunkley et al. 2008), the large scale distribution of galaxies (Cole et al. 2005; Tegmark et al. 2006) and by evidence of the accelerated expansion of the Universe from Supernovae observations (Astier et al. 2006; Wood-Vasey et al 2007), requires that the Universe is spatially flat, with a corresponding critical density, 30 percent of which consists of physical matter. However these observations also indicate that only 4 percent of this matter is baryonic in nature, implying that the remaining 26 percent consists of an elusive, non-baryonic component called dark matter, because of the severe constraints that current astronomical data set on its radiative capabilities.

Despite this compelling evidence for the existence of dark matter, its precise nature is still a topic of fierce debate. Particle physicists have independently supported dark matter by postulating the existence of a variety of exotic particles with wide-ranging properties which may potentially solve problems in particle physics whilst resulting in a relic particle density consistent with current observational constraints.

The most intensely studied dark matter candidate is the lightest neutralino (Bertone, Hooper & Silk 2005), a weakly-interacting massive particle (WIMP) motivated by supersymmetric extensions of the Standard Model of particle physcs. In many of these extensions the neutralino is the lightest supersymmetric particle (LSP). In theories where the LSP is stable, for example theories where R-Parity is a conserved quantum number (Weinberg 1982; Hall & Suzukit 1984; Allanach, Dedes & Dreiner 1999), the neutralino is thus a highly-motivated dark matter candidate. Further, an attractive feature of neutralinos is that a large region of the relevant supersymmetric parameter space can be investigated using CERN's Large Hadron Collider (LHC), scheduled for activation in 2008[1].

Whilst neutralino dark matter is 'cold', owing to its negligible free-streaming length (i.e. the length scale below which fluctuations in dark matter density are suppressed), warm dark matter (WDM) is typically lighter and possesses a much longer free-streaming length. WDM is a viable alternative to cold dark matter (CDM) models which may potentially resolve several shortfalls of the standard CDM model, like for example the over-prediction of low mass satellites and the existence of cuspy halos (Hogan & Dalcanton 2000; Dalcanton & Hogan 2001; Avila-Reese et al. 2001; Colín, Valenzuela, & Avila-Reese 2008). Among WDM candidates there are sterile neutrinos (Dodelson & Widrow 1994; Asaka, Blanchet & Shaposhnikov 2005; Asaka & Shaposhnikov 2005), majorons (Akhmedov, Berezhiani & Senjanovic 1992;

⋆ dtc@astro.ox.ac.uk
† mxl@astro.ox.ac.uk
‡ silk@astro.ox.ac.uk

[1] www.cern.ch/LHC

Berezinsky & Valle 1993; Lattanzi & Valle 2007) and light dark matter (LDM) particles (Boehm & Fayet 2004). What makes LDM interesting for this study is the fact that it can self-annihilate, as opposed to other forms of WDM, and therefore its annihilation rate can be enhanced by overdensities.

In this paper we re-examine the influence of neutralino and LDM annihilations on the thermal history of the Universe at times between the epochs of recombination and reionisation, referred to as the "Dark Ages", when gas existed in a nearly uniform, dark, neutral state. The investigation of the Dark Ages is one of the frontiers of modern cosmology, and will be carried on by a new generation of radio interferometers, such as LOFAR[2], MWA[3], 21 CMA[4], and SKA[5]. These experiments will look for the redshifted 21 cm signal associated with the hyperfine triplet-singlet transition of neutral hydrogen. If dark matter annihilates or decays, the resulting products subsequently collide and heat surrounding gas, increasing its kinetic temperature and ionised fraction, which in turn is manifested as distinct features in the 21 cm background signal that can be used to constrain the properties of dark matter (Furlanetto, Oh & Pierpaoli 2006; Shchekinov & Vasiliev 2007; Valdés et al. 2007).

With the exception of the very recent work by Chuzhoy (2007), past studies proclaim that the heating effects associated with the annihilation of WIMP dark matter are too small to be detected by current radio interferometers. However, these studies overlook the enhancements to the dark matter annihilation rate in galactic halos and in their substructures (Taylor & Silk 2003), which could be large enough to make the dark matter signature detectable by the next generation radio telescopes. In this paper we calculate the effect of neutralino and LDM annihilations on the 21 cm signal when accounting for the effect of dark matter clustering.

The rest of this paper is organized as follows. In § 2 we elaborate on the basic properties of neutralinos and LDM. We also discuss the basic physics describing the way in which energy from annihilations is injected into the intergalactic medium (IGM). In § 3 and § 4 we calculate the enhancement in the dark matter annihilation rate caused by the presence of halos and their substructures. In § 5 we estimate how much of the energy produced in a single dark matter annihilation is actually injected into the IGM. In § 6 we discuss the modifications to the differential equations describing the evolution of the ionised fraction and kinetic temperature of the IGM and subsequently use these equations to calculate the modified 21 cm background. In § 7 we calculate the predicted 21 cm background for our benchmark neutralino and LDM models and compare the results to the expected sensitivity of LOFAR, in order to assess the potential for a detection. Finally, in § 8 we summarise our results and draw our conclusions.

2 DARK MATTER CANDIDATES

The lightest supersymmetric (SUSY) neutralino is a superposition of higgsinos, winos and binos. Consequently neutralinos are electrically neutral and colourless, only interacting weakly and gravitationally and making them very difficult to detect directly. In SUSY models that conserve R-parity, the LSP is stable (Weinberg 1982; Hall & Suzukit 1984; Allanach et al. 1999). Consequently, in a scenario where present-day CDM exists as a result of thermal-freeze out, the dominant species of CDM could quite possibly include the LSP. The relic density of the LSP will then heavily depend on its mass and annihilation cross-section. Throughout this paper we assume that the LSP is the lightest SUSY neutralino. The neutralino is a popular candidate for CDM because the theoretically-motivated values of these parameters correspond to relic densities which are of the same order as current measurements for $\Omega_{\rm CDM}$ (for a more detailed review of the various properties and motivations for neutralino dark matter see e.g. Bertone et al. (2005)).

Neutralinos possess a wide-range of annihilation spectra owing to the vast extent of currently available SUSY parameter space. If the neutralino is lighter than the $W^{\pm}$ and Z bosons, annihilations will be dominated by the process $\chi\chi \to b\bar{b}$ with a minor contribution by $\chi\chi \to \tau^{+}\tau^{-}$. Assuming annihilations are dominated by the former process, the resulting spectrum will depend entirely on the LSP mass. For heavier LSPs, the annihilation products become more complex, often determined by several dominant annihilation modes including $\chi\chi \to W^{+}W^{-}$, $\chi\chi \to ZZ$ or $\chi\chi \to t\bar{t}$ as well as $\chi\chi \to b\bar{b}$ and $\chi\chi \to \tau^{+}\tau^{-}$.

The other dark matter candidate we are considering is LDM, consisting of MeV mass particles, which annihilate to electron-positron pairs [6] and consequently were considered to be a possible source of the positrons contributing to the 511 keV positronium decay signature from the centre of the galaxy observed by SPI/INTEGRAL (Knödlseder et al. 2005). Relevant analyses of this emission impose the constraint on the LDM mass $m_{\rm DM} < 20\,{\rm MeV}$ in order not to overproduce detectable gamma-rays from inner bremsstrahlung processes (Beacom, Bell & Bertone 2005) (although see Boehm & Uwer (2006)). A stronger, albeit less conservative constraint, $m_{\rm DM} < 3\,{\rm MeV}$ can be obtained if one considers the generation of gamma-rays from the in-flight annihilation between positrons produced from LDM annihilation and electrons residing in the interstellar medium of our galaxy (Beacom & Yuskel 2003).

Both in the case of neutralinos and LDM, the average rate of energy absorption per hydrogen atom in the IGM at a redshift z is given by

$$\dot{\epsilon} = \frac{1}{2} f_{\rm abs} \frac{n_{\rm DM,0}^{2}}{n_{\rm H,0}} \langle \sigma_{\rm ann} \upsilon \rangle m_{\rm dm} (1+z)^{3}\, C(1+z) \qquad (1)$$

where $m_{\rm DM}$ is the mass of the dark matter particle, $\langle \sigma_{\rm ann.} \upsilon \rangle$

---

[2] http://www.lofar.org
[3] http://www.haystack.mit.edu/ast/arrays/mwa
[4] http://web.phys.cmu.edu/past/
[5] http://www.skatelescope.org

[6] MeV LDM particles can also potentially annihilate directly into neutrinos and photons. However most theories suppress this emission in order to be consistent with observational constraints. Here we only consider scenarios where LDM annihilates entirely to electron positron pairs, so that our results can be considered as an upper limit to the more general case.

is the thermally-averaged dark matter annihilation cross-section, $n_{\rm DM,0}$ and $n_{\rm H,0}$ are the current *average* number densities of dark matter and hydrogen respectively, and $f_{\rm abs.}$ is the fraction of energy which is absorbed by the IGM. $C(1+z)$ is the redshift-dependent enhancement of the annihilation rate owing to dark matter structures, relative to a completely homogeneous Universe. [7]

3 EXTRAGALACTIC DARK MATTER ANNIHILATION RATE

In the standard cosmological model all structure in the universe originated from small amplitude quantum fluctuations during an epoch of inflationary expansion shortly after the Big Bang. The linear growth of the resulting density fluctuations is then completely determined by their initial power spectrum, which for ΛCDM is usually assumed to be a power law with spectral index n. Current limits on n from observations of temperature fluctuations in the Cosmic Microwave Background conducted by the Wilkinson Microwave Anisotropy Probe, $n_{\rm WMAP} = 0.963^{+0.014}_{-0.015}$ (Dunkley et al. 2008), supports the existence of a power spectrum consistent with inflation.

During the expansion of the Universe, the small initial density fluctuations will eventually grow and produce the structures we observe today. In the currently accepted cosmological model, smaller structures form first and then merge to form larger ones in a process of "bottom-up" hierarchical structure formation. The mass distribution at any given redshift can potentially be determined through the use of numerical simulations.

As a first approximation, the smaller progenitors forming larger isolated structures are completely disrupted after merging and the resulting 'smooth' dark matter density distribution can be described by a continuous function conventionally of the form

$$\rho(r) = \frac{\rho_s}{(r/r_s)^\gamma \left[1+(r/r_s)^\alpha\right]^{(\beta-\gamma)/\alpha}} \qquad (2)$$

where r is the distance from the centre of the halo (spherically symmetrical), r_s is a scale radius, ρ_s is a normalisation factor, and α, β and γ are free parameters.

However, N-body simulations of CDM halos reveal that a wealth of substructure halos (subhalos henceforth) exists within such halos. Moreover, Diemand et al. (2008) recently claimed, based on the results of the second generation of Via Lactea simulations, that a further generation of sub-subhalos exists with a self-similar mass distribution relative to the parent subhalo. This suggests the possibility that if one were to conduct simulations with sufficiently high resolution, one would find a long nested self-similar series of halos within halos within halos etc., all the way down to the smallest halos.

This intriguing result has significant implications for the indirect detection of annihilating dark matter, since the rate of dark matter annihilations is proportional to the square of the local density, hence the presence of over-densities can significantly increase the annihilation rate relative to that obtained with a smooth background distribution.

The above scenario applies to structures formed in a CDM-dominated Universe. In a WDM-dominated Universe, the significant damping of small-scale density fluctuations, due to the larger free-streaming length, should be taken into account. Following Bardeen et al. (1986) this can be accounted for by using the modified power spectrum

$$P(k) = T^2_{\rm WDM}(k) P_{\Lambda{\rm CDM}}, \qquad (3)$$

where the WDM transfer function is approximated by

$$T_{\rm WDM}(k) = \exp\left[-\frac{kR_f}{2} - \frac{(kR_f)^2}{2}\right], \qquad (4)$$

where R_f is the free-streaming length.

For WDM particles with negligible interaction rates the free-streaming length is related to the particle mass $m_{\rm DM}$ by (Bardeen et al. 1986)

$$R_{f,n} = 7.4\times10^{-6}\left(\frac{m_{\rm dm}}{1\,{\rm MeV}}\right)^{-4/3}\left(\frac{\Omega_{\rm DM}}{0.258}\right)^{1/3} \times \left(\frac{h}{0.719}\right)^{5/3} h^{-1}\,{\rm Mpc}. \qquad (5)$$

However, the interaction rates for self-annihilating LDM in the models we consider are non-negligible. In this case, the free-streaming length is given by (Boehm & Schaeffer 2005)

$$R_{f,i} = 0.3\left(\frac{\Gamma_{\rm dec,DM}}{6\times10^{-24}\,{\rm s}^{-1}(1+z_{\rm dec.})^3}\right)^{1/2} \times \left(\frac{1\,{\rm MeV}}{m_{\rm DM}}\right)^{1/2} {\rm Mpc}, \qquad (6)$$

where $\Gamma_{\rm dec,DM}$ is the WDM self-annihilation rate at the decoupling redshift $z_{\rm dec.}$

$$\Gamma_{\rm dec.,DM} = \frac{1}{2}\frac{\rho_{c,0}\Omega_{\rm DM,0}}{m_{\rm DM}}\langle\sigma_{\rm ann.}v\rangle_{\rm dec.}(1+z_{\rm dec})^3, \qquad (7)$$

where $\langle\sigma_{\rm ann.}v\rangle_{\rm dec.}$ is the thermally-averaged product of the WDM annihilation cross-section multiplied by relative speed evaluated at the $z_{\rm dec}$, which in order to obtain the correct relic density today is required to be approximately $\langle\sigma_{\rm ann.}v\rangle_{\rm dec.} \sim 10^{-26}{\rm cm}^3{\rm s}^{-1}$.

For $m_{\rm DM} = 3\,{\rm MeV}$, $R_{f,n} = 2.38\,{\rm pc}$ and $R_{f,i} = 97.99\,{\rm pc}$, while for $m_{\rm DM} = 20\,{\rm MeV}$, $R_{f,n} = 0.190\,{\rm pc}$ and $R_{f,i} = 14.70\,{\rm pc}$. Hence, in both cases the comoving free-streaming length set by interactions is at least an order of magnitude larger than that when interactions are completely negligible, and consequently we must invoke the former in our determination of the cut-off scale in the WDM power spectrum.

We follow Avila-Reese et al. (2001) and define a characteristic free-streaming wavenumber k_f such that $T_{\rm WDM}(k_f) \simeq 0.5$ leading to $k_f \simeq 0.46/R_f$. This wavenumber is then related to a characteristic filtering mass M_f by

$$M_f = \frac{4\pi}{3}\bar{\rho}_{\rm WDM}\left(\frac{\lambda_f}{2}\right)^3, \qquad (8)$$

---

[7] The factor of 1/2 in eq. (1) assumes Dirac dark matter particles; for Majorana particles this should be further multiplied by a factor of 2.

where $\lambda_f = 2\pi/k_f = 13.6R_f$. In this paper we invoke the approximation $M_{\rm min.} \sim M_f$, where here $M_{\rm min.}$ is the minimum mass of a LDM halo, and equal to approximately $46\,M_\odot$ and $0.16\,M_\odot$ for $m_{\rm dm} = 3\,{\rm MeV}$ and $20\,{\rm MeV}$ respectively. Since the mass within a given comoving volume is constant as the Universe expands, the result (8) is independent of redshift.

Below we perform a series of detailed calculations illustrating the enhancement of the annihilation rate relative to that obtained with a completely smooth Universe, known as the *clumping factor*.

4 CALCULATION OF THE CLUMPING FACTOR

We assume a standard homogeneous, isotropic Universe with a flat spatial geometry. Let $R(M, z)$ be the average annihilation rate *per baryon* in a generic dark matter halo of mass M located at redshift z. Even for large M, this source can be regarded as an unresolved point-source and we assume this throughout for all halos considered. The rate of annihilations at a given redshift is then equal to

$$\Gamma(z) = (1+z)^3 \int_{M_{\rm min.}}^{M_{\rm max.}} {\rm d}M \frac{{\rm d}n}{{\rm d}M}(M,z)R(M,z) \tag{9}$$

where we have introduced the unconditional halo mass function, ${\rm d}n/{\rm d}M$, i.e. the comoving number density of virialised halos with mass M located at redshift z, (the factor $(1+z)^3$ converts this from comoving to proper density). The integral spans over the mass range $M > M_{\rm min.}$, where $M_{\rm min.}$ can be as small as $10^{-12}M_\odot$ due to kinetic decoupling in the case of CDM (Profumo et al. 2006), and approximated by the filtering mass (8) in the case of WDM.

Three ingredients are required in order to calculate the annihilation rate (9). We need to specify the annihilation cross-section of our dark matter candidates (in our case neutralinos or LDM). Secondly, we need to specify the dark matter density profile of a generic halo of mass M at redshift z. Finally we need an estimate of the distribution of halos, i.e. an estimate of the halo mass function ${\rm d}n(M, z)/{\rm d}M$.

4.1 The halo mass function

Press-Schechter theory (Press & Schechter 1974) postulates that the cosmological mass function of dark matter halos can be expressed in the universal form

$$\frac{{\rm d}n}{{\rm d}M} = \frac{\bar{\rho_0}}{M^2}\nu f(\nu)\frac{{\rm dlog}\nu}{{\rm dlog}M} \tag{10}$$

where $\bar{\rho_0}$ is the average comoving dark matter density $\bar{\rho_0} = \rho_c\Omega_M$, where ρ_c is the present critical density of the Universe. The parameter $\nu = \delta_{sc}/\sigma(M)$, is defined as the ratio of the critical overdensity required for spherical collapse at redshift z, extrapolated using linear theory to present time, and $\sigma(M)$, the r.m.s. of primordial density fluctuations when smoothed on a scale which contains mass M, again extrapolated using linear theory to present time. The form of $\delta_{sc}(z)$ can be found in Tegmark et al. (2005). $\sigma(M)$ is related to the power spectrum $P(k)$ of the linear density field extrapolated to present time by

$$\sigma^2(M) = \int {\rm d}^3k W^2(kR)P(k), \tag{11}$$

where W is the top-hat window function at the scale $R = (3M/4\pi\bar{\rho})^{1/3}$ where $\bar{\rho}$ is the mean matter density. We utilise the analytical approximation specified in Tegmark et al. (2006), relevant in the linear regime long after the relevant fluctuation modes have entered the horizon, when all modes grow at the same rate, which means that $\sigma(M)$ can be factored as a product of two functions, one solely dependent on redshift z and the other solely dependent on the comoving spatial scale R. We normalise P and σ by computing σ at $R = 8h^{-1}$ Mpc and setting the result equal to the cosmological parameter σ_8 as measured by WMAP, $\sigma_8 = 0.796\pm0.036$ (Dunkley et al. 2008).

The first-crossing distribution $f(\nu)$ has the following analytical fit (Sheth & Tormen 2002) to the N-body simulation results from the Virgo consortium (Jenkins et al. 1998)

$$\nu f(\nu) = A\left[1 + (a\nu)^{-p}\right]\left(\frac{a\nu}{2\pi}\right)^{1/2}\exp\left(-\frac{a\nu}{2}\right) \tag{12}$$

where the parameters $p = 0.3$, and $A = 0.32218$ are determined by the requirement that all mass lies within a given halo, i.e. $\int {\rm d}\nu f(\nu) = 1$ or equivalently $\int {\rm d}MM{\rm d}n/{\rm d}M = \bar{\rho}_0$.

4.2 The density profile of dark matter halos

Since the rate of dark matter annihilation scales with density squared, it sensitively depends on the density profile of each halo. We consider three universal density profiles to model the smooth distribution of dark matter within each halo (substructure will be dealt with later in this section). Firstly we consider the popular profile proposed by Navarro, Frenk & White (1996, 1997) (NFW),

$$\rho(r) = \frac{\rho_s}{(r/r_s)\left[1 + (r/r_s)\right]^2} \tag{13}$$

which corresponds to $\alpha = 1$, $\beta = 3$ and $\gamma = 1$ in eq.(2). Secondly, we consider a profile with a significantly larger slope, specifically the one proposed by Moore et al. (1999).

$$\rho(r) = \frac{\rho_s}{(r/r_s)^{1.5}\left[1 + (r/r_s)^{1.5}\right]} \tag{14}$$

which corresponds to $\alpha = 1.5$, $\beta = 3$ and $\gamma = 1.5$. Both of these profiles have the same functional form and are both singular towards the galactic centre (in fact, the slope of the Moore profile must necessarily be truncated for $r < r_{\rm min.}$, where $r_{\rm min.} \sim 0$ (see below), otherwise the integral of density squared diverges.

However, there have been indications that cuspy profiles are inconsistent with observations, specifically regarding the rotation curves of small-scale galaxies (Flores & Primack 1994; Moore 1994; Weldrake, de Blok & Walter 2003; Donato, Gentile & Salucci 2004; Gentile et al. 2007), which are more likely to be consistent with density profiles possessing flattened cores similar to that which may be achieved with WDM (Hogan & Dalcanton 2000; Colin et al. 2008).

Therefore, we lastly consider the Burkert density profile (Burkert 1995)

$$\rho(r) = \frac{\rho_s}{[1+(r/r_s)]\,[1+(r/r_s)^2]} \tag{15}$$

which has been shown to be fairly consistent with the rotation curves of a large number spiral galaxies (Salucci & Burkert 2000).

4.3 Concentration - mass relation for dark matter halos

Here we introduce the virial concentration parameter $c_{\rm vir.}$, defined by

$$c_{\rm vir.} = \frac{r_{\rm vir.}}{r_s}, \tag{16}$$

where r_s is the scale radius defined above and $r_{vir.}$ is the virial radius of the halo, defined to be the radius encapsulating the virial mass M of the halo within which the average density is equal to the overdensity $\Delta_{\rm vir.}$ times the average cosmological density $\bar{\rho}(z)$ at that redshift

$$M = \frac{4\pi}{3}\Delta_{vir.}\bar{\rho}(z) r^3_{\rm vir.}. \tag{17}$$

For $\Delta_{\rm vir.}$ we use the approximation given in Tegmark et al. (2006)

$$\Delta_{\rm vir.} \simeq 18\pi^2 + 52.8x^{0.7} + 16x, \tag{18}$$

where $x(z) = \Omega_\Lambda(z)/\Omega_M(z)$, ($\Delta_{\rm vir.} \simeq 311$ at $z = 0$ for $\Omega_M = 0.3$ ad $\Omega_\Lambda = 0.7$) and accurate to within 4% of the exact numerical calculation at relevant times.

There has been evidence from simulations revealing a strong correlation between the halo mass M and its corresponding concentration $c_{\rm vir.}$, with larger concentrations in smaller mass halos, which is consistent with the idea of bottom-up hierarchical structure formation with smaller halos collapsing at earlier times when the average density of the Universe was much greater (Navarro et al. 1996, 1997). This relationship was later reaffirmed by Bullock et al. (2001) (B2001 hereafter) using a sample of simulated halos in the mass range $10^{11} < M/h^{-1}M_\odot < 10^{14}$, who proposed a toy model to describe this behaviour, which is popular in the relevant literature: On average, a collapse redshift z_c is assigned to each halo of mass M through the relation $M_* = FM$, where at a redshift z the typical collapsing mass $M_*(z)$ is defined implicitly by the relation $\sigma(M_*(z)) = \delta_{sc}(z)$ and is postulated to be a fixed fraction F of M, which following Ullio et al. (2002) we set equal to 0.015. The density of the Universe at redshift z_c is then associated with a characteristic density of the halo at z. Therefore, here we use the average concentration-mass relation obtained using the above method, which is given by

$$c_{\rm vir.}(M,z) = K\frac{1+z_c}{1+z} = \frac{c_{\rm vir.}(M, z=0)}{1+z} \tag{19}$$

where $K \simeq 5$, for $\Omega_\Lambda = 0.742$, $\Omega_M = 0.258$, $h = 0.719$ and $\sigma_8 = 0.796$ (Dunkley et al. 2008).

4.4 Clumping factor for smooth halos

We are now in a position to be able to calculate the clumping factor $C(1+z)$ attributed to extragalactic halos with smooth density profiles described by equations (13)-(15), with concentrations given by equation (19).

We start by writing down the annihilation rate $R(M,z)$ within a dark matter halo of mass M located at redshift z, given by

$$R(M,z) = \frac{1}{2}\frac{\langle\sigma_{\rm ann.}\upsilon\rangle}{m^2_{\rm DM}\bar{n}_b(z)}\int\limits_{r=0}^{r_{\rm vir.(M,z)}} \rho^2(r) 4\pi r^2 {\rm d}r. \tag{20}$$

where $\langle\sigma_{\rm ann.}\upsilon\rangle$ is the thermally-averaged product of the dark matter annihilation cross-section multiplied by relative speed, and $\bar{n}_b(z)$ is the average cosmological baryon density at redshift z. For a halo of mass M with an NFW profile with concentration $c_{\rm vir.}(M,z)$, $R(M,z)$ is easily calculated to be

$$\begin{aligned} R(M,z) &= \frac{1}{2}\frac{\langle\sigma_{\rm ann.}\upsilon\rangle}{\bar{n}_b(z)}\left(\frac{\rho_s}{m_{\rm DM}}\right)^2 \frac{4\pi}{3}\left(\frac{r_{\rm vir.}(z,M)}{c_{\rm vir.}(z,M)}\right)^3 \\ &= \times\left\{1 - \frac{1}{[1+c_{\rm vir.}(M,z)]^3}\right\}. \end{aligned} \tag{21}$$

By equating (17) for the virial mass M to the integral

$$\begin{aligned} M &= \int\limits_{r=0}^{r_{\rm vir.}} \rho(r, c_{\rm vir.}(M,z)) 4\pi r^2 {\rm d}r \\ &= 4\pi\left(\frac{r_{\rm vir.}}{c_{\rm vir.}(M,z)}\right)^3 \rho_s(M,z) \\ &\quad \times\left[\log\left(1+c_{\rm vir.}(z,M)\right) - \left(\frac{c_{\rm vir.}(z,M)}{(1+c_{\rm vir.}(z,M))}\right)\right] \end{aligned} \tag{22}$$

we obtain the relation for the scale density

$$\begin{aligned} \rho_s(M,z) &= \frac{M}{4\pi\left(\frac{r_{\rm vir.}}{c_{\rm vir.}(M,z)}\right)^3} \\ &\times \frac{1}{\left[\log\left(1+c_{\rm vir.}(z,M)\right) - \left(\frac{c_{\rm vir.}(z,M)}{(1+c_{\rm vir.}(z,M))}\right)\right]} \end{aligned} \tag{23}$$

For the Burkert profile, it is not possible to express the results corresponding to equations (22) and (23) in analytical form. For the Moore profile, in order for the integral over density squared to be finite we must truncate the density below a radius $r_{\rm min.}$. Defining the variable $x = rc_{\rm vir.}/r_{\rm vir.}$ with $x_{\rm min.} = r_{\rm min.}c_{\rm vir.}/r_{\rm vir.}$, expressions corresponding to (22) and (23) for the Moore profile

$$\begin{aligned} \rho(r) &= \frac{\rho_s}{(r/r_s)^{1.5}\,[1+(r/r_s)^{1.5}]} \quad \text{for} \quad r > r_{\rm min.} \\ \rho(r) &= \rho(r_{\rm min.}) \quad \text{for} \quad r < r_{\rm min.} \end{aligned} \tag{24}$$

are calculated as

$$
\begin{aligned}
R(M,z) &= \frac{1}{2}\frac{\langle\sigma_{\mathrm{ann.}}\upsilon\rangle}{\bar{n}_b(z)}\left(\frac{\rho_s}{m_{\mathrm{DM}}}\right)^2\frac{4\pi}{3}\left(\frac{r_{\mathrm{vir.}}(z,M)}{c_{\mathrm{vir.}}(z,M)}\right)^3\\
&\times\ F_1(c_{\mathrm{vir.}},x_{\mathrm{min.}}),
\end{aligned}
\tag{25}
$$

where

$$
\begin{aligned}
F_1(c_{\mathrm{vir.}},x_{\mathrm{min.}}) &= \frac{1}{3}\frac{1}{(1+x_{\mathrm{min.}})^2}\\
&+\ \frac{1}{1.5}\left[\log\left(\frac{c_{\mathrm{vir.}}^{1.5}(1+x_{\mathrm{min.}}^{1.5})}{x_{\mathrm{min.}}^{1.5}(1+c_{\mathrm{vir.}}^{1.5})}\right)\right]\\
&+\ \frac{1}{1.5}\left[\frac{1}{1+c_{\mathrm{vir.}}^{1.5}}-\frac{1}{1+x_{\mathrm{min.}}^{1.5}}\right]
\end{aligned}
\tag{26}
$$

and

$$
\begin{aligned}
\rho_s(M,z) &= \frac{M}{4\pi\left(\frac{r_{\mathrm{vir.}}}{c_{\mathrm{vir.}}(M,z)}\right)^3}\\
&\times\ \left[\frac{1}{1.5}\log\left(\frac{1+c_{\mathrm{vir.}}^{1.5}}{1+x_{\mathrm{min.}}^{1.5}}\right)+\frac{1}{3}\frac{x_{\mathrm{min.}}^{1.5}}{(1+x_{\mathrm{min.}}^{1.5})}\right]^{-1}\\
&\equiv\ \frac{M}{4\pi\left(\frac{r_{\mathrm{vir.}}}{c_{\mathrm{vir.}}(M,z)}\right)^3F_2(c_{\mathrm{vir.}},x_{\mathrm{min.}})}.
\end{aligned}
\tag{27}
$$

respectively.

Then following equation (9) for the contribution to the dark matter annihilation rate per baryon $\Gamma_{\mathrm{halos}}(z)$ by halos located at redshift z, we obtain

$$
\begin{aligned}
\Gamma_{\mathrm{halos}}(z) &= (1+z)^3\int_{M_{\mathrm{min.}}}^{M_{\mathrm{max.}}}\mathrm{d}M\frac{\mathrm{d}n}{\mathrm{d}M}(M,z)R(M,z)\\
&= \frac{1}{2}\frac{\langle\sigma_{\mathrm{ann.}}\upsilon\rangle}{m_{\mathrm{DM}}^2\bar{n}_b(z)}(1+z)^3\\
&\times\int_{M_{\mathrm{min.}}}^{M_{\mathrm{max.}}}\mathrm{d}M\frac{\mathrm{d}n}{\mathrm{d}M}(M,z)\int_{r=0}^{r_{\mathrm{vir.(M,z)}}}\rho^2(r)4\pi r^2\mathrm{d}r.
\end{aligned}
\tag{28}
$$

To calculate $r_{\mathrm{min.}}$ for the Moore profile we adopt the following method: Within some minimum radius we assume that most of the neutralino dark matter that we are considering would have self-annihilated, leaving a flattened density core. The size of the core will depend on several time-scales: the time-scale for a single dark matter annihilation (per particle) $t_{\mathrm{ann.}}\sim(n_\chi\langle\sigma\upsilon\rangle)^{-1}$, the average time-scale for the replenishment of an annihilated dark matter particle within the core owing to in-falling dark matter from larger radii $t_{\mathrm{in.}}$, and the collapse time-scale of the halo in question $t_{\mathrm{coll}}\ll t_h$, where $t_h\sim10^{17}$s is the Hubble time. Clearly, for a core to be produced the average time-scale for replenishment of a dark matter particle within the core must be more than the time it takes to annihilate, and must be much smaller than the time-scale for the formation of the halo, which if the halo is to exist must be much smaller than the Hubble time. Hence for a core to form we require the condition

$$
n_\chi\langle\sigma\upsilon\rangle\gg\frac{1}{t_{\mathrm{in.}}}\gg\frac{1}{t_{\mathrm{coll.}}}\gg\frac{1}{t_h}.
\tag{29}
$$

Here, we adopt the conservative criterion $(\rho_\chi(r_{\mathrm{min.}})/m_\chi)\langle\sigma\upsilon\rangle\ \sim\ t_h^{-1}$, with canonical values of the neutralino mass and annihilation cross-section of $m_\chi\sim100\,\mathrm{GeV}$ and $\langle\sigma\upsilon\rangle\sim10^{-26}\mathrm{cm}^3\mathrm{s}^{-1}$. Since the Moore profile is monotonically decreasing with increasing radius, this sets an upper limit for $x_{\mathrm{min.}}$ which is approximately equal to 10^{-8} for the Milky Way at present day, which is consistent with similar approximations by other authors (e.g. see Taylor & Silk (2003)).

The corresponding rate of dark matter annihilation per unit volume contributed by the smooth background density at redshift z is given by

$$
\Gamma_{\mathrm{smooth}}(z)=\frac{1}{2}\frac{\langle\sigma_{\mathrm{ann.}}\upsilon\rangle}{\bar{n}_b(z)}\bar{\rho}_{\mathrm{DM}}^2(z),
\tag{30}
$$

where $\rho_{\mathrm{DM}}(z)=\rho_{c,0}\Omega_{\mathrm{DM},0}(1+z)^3$. Therefore, we define the *clumping factor* for smooth halos $C_{\mathrm{halo}}(z)$ as

$$
\begin{aligned}
C_{\mathrm{halo}}(z) &= 1+\frac{\Gamma_{\mathrm{halo}}(z)}{\Gamma_{\mathrm{smooth}}(z)}\\
&= 1+\frac{(1+z)^3}{\bar{\rho}_{\mathrm{DM}}^2(z)}\int\mathrm{d}M\frac{\mathrm{d}n}{\mathrm{d}M}(M,z)\\
&\times\int_{r=0}^{r_{\mathrm{vir.(M,z)}}}\rho^2(r)4\pi r^2\mathrm{d}r,
\end{aligned}
\tag{31}
$$

where $C_{\mathrm{halo}}(z)\rightarrow1$ for a completely smooth Universe. For halos with NFW profiles, using equations (21), (23), (28) and (30) we obtain

$$
\begin{aligned}
&C_{\mathrm{halo}}(z)=1+\\
&\quad\frac{(1+z)^3}{\bar{\rho}_{\mathrm{DM}}^2(z)}\int\mathrm{d}M\frac{\mathrm{d}n}{\mathrm{d}M}(M,z)\rho_s^2(M,z)\\
&\quad\times\frac{4\pi}{3}\left(\frac{r_{\mathrm{vir.}}(M,z)}{c_{\mathrm{vir.}}(M,z)}\right)^3\left[1-\frac{1}{(1+c_{\mathrm{vir.}}(M,z))^3}\right],
\end{aligned}
\tag{32}
$$

whilst for halos possessing a Moore profile, using equations (25), (26), (27), (28) and (30) we obtain

$$
\begin{aligned}
&C_{\mathrm{halo}}(z)=1+\\
&\quad\frac{(1+z)^3}{\bar{\rho}_{\mathrm{DM}}^2(z)}\int\mathrm{d}M\frac{\mathrm{d}n}{\mathrm{d}M}(M,z)\rho_s^2(M,z)\\
&\quad\times\frac{4\pi}{3}\left(\frac{r_{\mathrm{vir.}}(M,z)}{c_{\mathrm{vir.}}(M,z)}\right)^3F_1(c_{\mathrm{vir.}}(M,z),x_{\mathrm{min.}}(M,z)).
\end{aligned}
\tag{33}
$$

Since the integrals over powers of the Burkert density profile are non-analytical we do not attempt to simplify its corresponding expression for C_{halo} beyond equation (31).

In figures 1-3 we display plots of $C_{\mathrm{halo}}(z)$ as a function of z for halos with (a) NFW profiles, (b) Moore profiles and (c) Burkert profiles.

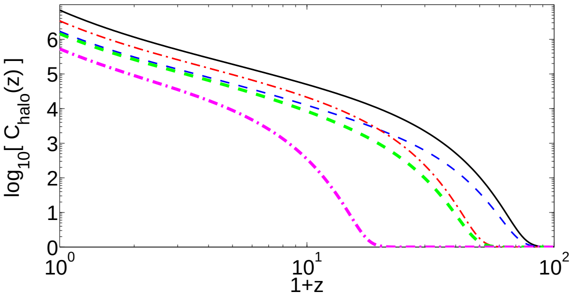

Figure 1. Clumping factor as a function of redshift for dark matter halos with mass $M > M_{\rm min.}$ with smooth NFW density profiles with a $c_{\rm vir.} - M$ relation described by eq. (19), truncated at a halo mass $M_{\rm cut}$. The displayed curves correspond to values of $(M_{\rm min.}/M_\odot, M_{\rm cut}/M_\odot)$ equal to $(10^{-12}, 10^{-12})$ (thin black solid), $(10^{-12}, 10^6)$ (thin blue dashed), $(10^{-4}, 10^{-4})$ (thin red dot-dashed), $(10^{-4}, 10^6)$ (thick green dashed),and $(10^6, 10^6)$ (thick magenta dot-dashed).

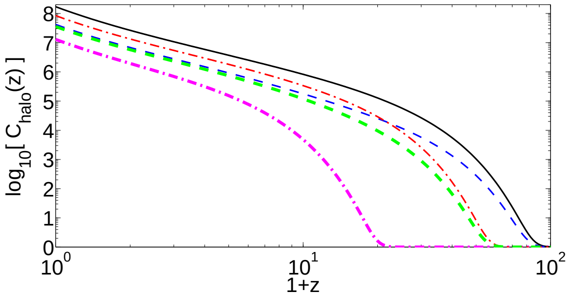

Figure 2. Same as for figure 1, except now for halos possessing Moore density profiles.

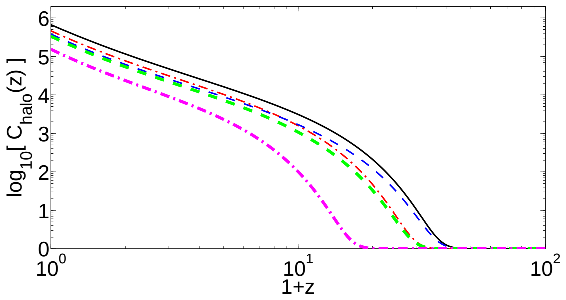

Figure 3. Same as for figure 1, except now for halos possessing Burkert density profiles for values of $(M_{\rm min.}/M_\odot, M_{\rm cut}/M_\odot)$ equal to $(0.16, 0.16)$ (thin black solid), $(0.16, 10^6)$ (thin blue dashed), $(46, 46)$ (thin red dot-dashed), $(46, 10^6)$ (thick green dashed) and $(10^6, 10^6)$ (thick magenta dot-dashed).

Halos with cuspy density profiles, such as the NFW and Moore profiles, are typical of CDM halos for which the minimum mass cut-off scale in the matter power spectrum is determined by collisional damping and free streaming in the early Universe. For WIMP dark matter the value of $M_{\rm min.}$ can range from $10^{-12} M_\odot$ to $10^{-4} M_\odot$ for typical kinetic decoupling temperatures. Hence in Figs. 1 and 2 we illustrate the effect on the clumping factor for values of $M_{\rm min.}$ of $10^{-12}, 10^{-4}$ and $10^6 M_\odot$, where the latter value is the typical minimum mass of resolved subhalos in simulations of galactic halos. We also demonstrate the influence of truncating the Bullock *et al.* concentration-mass relation (referred to as the "B2001 relation" hereafter) below a mass of $10^6 M_\odot$, aswell as using the relation when extrapolated to $M_{\rm min.}$.

In Fig. 3 we show the clumping factor for halos halos with flattened cores like the ones possibly formed by WDM. In particular, we plot $C_{\rm halo}$ for minimum halo masses $M_{\rm min.} \simeq 46\, M_\odot$ and $0.16 M_\odot$, corresponding to the values of the damping mass (8) obtained using $m_{\rm WDM} = 3\,{\rm MeV}$ and $m_{\rm WDM} = 20\,{\rm MeV}$, respectively. We also again illustrate the effect of using relation eq. (19) when extrapolated to $M_{\rm min.}$ or truncated at $10^6 M_\odot$. The selected values of $m_{\rm WDM}$ correspond to the respective upper limits on the LDM particle mass from constraints on inner bremsstrahlung gamma ray flux from the galactic centre (Beacom et al. 2005) (although see Boehm & Uwer (2006)), and from in-flight annihilation (Beacom & Yuskel 2003) between positrons from LDM annihilation and electrons in the interstellar medium.

4.5 Clumping factor for halos possessing sub-halos and sub-sub halos

Thus far we have considered the amplification of the dark matter annihilation rate for isolated halos with smooth density profiles. However, as already mentioned, N-body simulations indicate that a significant proportion of the smaller progenitors giving rise to larger mass halos survive the merging processes and the tidal forces exerted upon them during their orbital motion within halos. In particular, the most recent ΛCDM Via Lactea II simulations of galactic halos presented in Diemand et al. (2008) and in Kuhlen, Diemand & Madau (2008) (KDM hereafter), revealed a second generation of surviving substructures within halos (designated as "sub-subhalos"). Further, these simulations suggest that the mass distribution of sub-subhalos within their host subhalo is the same as the mass distribution of subhalos within their host halo.

Since the dark matter annihilation rate scales with density squared, such subhalos and sub-subhalos could provide significant enhancement to the annihilation rate even for modest substructure mass fractions within halos/subhalo. For halos of mass M these have been suggested to be as much as 10% for subhalo masses $M_{\rm s}$ in the range $10^{-5} < M_{\rm s}/M < 10^{-2}$ (Diemand et al. 2008) (which corresponds approximately to a constant mass fraction per subhalo mass decade of 3%, owing to the fact that the subhalo mass function has a slope of approximately 2, see below). However, owing to the fact that substructures invariably form earlier than their host halos, and that tidal disruption is unlikely to effect the inner density profiles of structures (i.e. where the majority of the enhancement originates), the concentration of substructures may be significantly greater than that of their host halos. The simulation results recently presented in KDM are consistent with the ratio $N_c = c_{\rm vir.}^{\rm halo}/c_{\rm vir.}^{\rm subhalo} \simeq 3$ for subhalos located at solar radii within galactic halos[8],

---

[8] Although N_c demonstrates a slight galactocentric radial dependence, the authors of KDM claim that the effect on the overall annihilation rate is negligible.

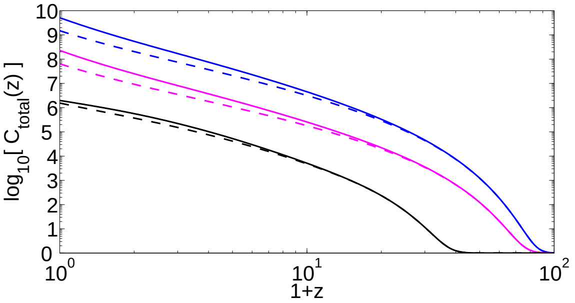

Figure 4. Plots of the total clumping factor from halos and subhalos, given by $C_{\rm total.}(z) = 1 + C_{\rm halos}(z) + C_{\rm subhalos}(z)$, where we have renormalised the contribution from halos to account for their finite mass fraction in the form of subhalos per subhalo mass decade $F_{\rm sub.}$ for varying values of the substructure mass function index β. Displayed are values of $C_{\rm total}$ for structures with NFW (purple) and Moore (blue) density profiles for $\beta = 2$ and 1.8 (solid and dashed curves respectively) and $\beta = 2$ and 1.6 for the Burkert profile (black solid and dashed curves respectively). We take $M_{\rm cut} = M_{\rm min.} = 10^{-12}\,M_\odot$ for NFW and Moore profiles and $0.16\,M_\odot$ for Burkert profiles. In all cases $F_{\rm sub.} = 3\%$, $N_c = 3$.

whilst the numerical simulations of Bullock *et al.* show that on average $N_c \simeq 1.5$ for halos of mass $M \sim 5\times10^{11}M_\odot$ (B2001).

Here we calculate the contribution to the clumping factor by halos possessing substructures with a self-similar mass distribution. Consider a dark matter halo of mass M with a subhalo mass distribution function given by

$$\frac{{\rm d}N(M)}{{\rm d}M_s} \propto M_s^{-\beta}, \tag{34}$$

where the index β is assumed to be time-independent and approximately equal to 2, i.e. equal mass per decade in subhalos (KDM).

There are indications that β may slightly deviate from this value, particularly for WDM substructures. Knebe et al. (2008) claim that β may be as small as 1.6. However, as shown in Fig. 4, the effect on the clumping factor of varying β deviating slightly from 2 is small. We therefore adopt the value $\beta = 2$ for both CDM and WDM. Consequently, each subhalo mass decade contributes a constant fraction $F_{\rm sub.}$ of the halo mass.

Adopting a course of reasoning analogous to that used to derive equation (20), the rate of annihilation within a similar halo, owing solely to subhalos within it, possessing smooth density profiles $\rho(r)$, is then given by

$$\begin{aligned} R_{\rm sub.}(M,z) &= \frac{\langle\sigma_{\rm ann.}\upsilon\rangle}{2m_{\rm DM}^2}\int {\rm d}M_s\frac{{\rm d}N(M,F_{\rm sub.})}{{\rm d}M_s} \\ &\times \int\limits_{r=0}^{r_{\rm vir.}(z,M_s)} \rho^2(r, c_{\rm vir.}^{\rm sub.}[M_s,z])4\pi r^2{\rm d}r \\ &= \frac{\langle\sigma_{\rm ann.}\upsilon\rangle}{2m_{\rm DM}^2}A(M,F_{\rm sub.})\int {\rm d}M_s M_s^{-\beta} \\ &\times \int\limits_{r=0}^{r_{\rm vir.}(z,M_s)} \rho^2(r, c_{\rm vir.}^{\rm sub.}[M_s,z])4\pi r^2{\rm d}r, \end{aligned} \tag{35}$$

where A is the appropriate normalisation of ${\rm d}N/{\rm d}M_s$, $\rho_s^{\rm sub.}$ is the subhalo scale density, which can be obtained from the previous expressions (23) or (27) for NFW and Moore profiles respectively with the substitutions $c_{\rm vir.} \to c_{\rm vir.}^{\rm sub.}$ and $M \to M_s$. Then integrating this contribution over all halos at redshift z we obtain the annihilation rate for all subhalos residing within such halos

$$\begin{aligned} \Gamma_{\rm subhalos}(z) &= \int {\rm d}M\frac{{\rm d}n(M,z)}{{\rm d}M}R_{\rm sub.}(M,z,F_{\rm sub}) \\ &= \frac{\langle\sigma_{\rm ann.}\upsilon\rangle}{2m_{\rm DM}^2} \\ &\times \int {\rm d}M\frac{{\rm d}n(M,z)}{{\rm d}M}A(M,F_{\rm sub.})\int {\rm d}M_s M_s^{-\beta} \\ &\times \int_{r=0}^{r_{\rm vir.}(z,M_s)} \rho^2(r, c_{\rm vir.}^{\rm sub.}[M_s,z])4\pi r^2{\rm d}r, \end{aligned} \tag{36}$$

and following equation (31), we obtain the associated subhalo clumping factor

$$\begin{aligned} C_{\rm subhalos} &= 1 + \frac{\Gamma_{\rm subhalos}(z)}{\Gamma_{\rm smooth}(z)} \\ &= 1 + \frac{(1+z)^3}{\bar\rho_{\rm DM}^2(z)}\int {\rm d}M\frac{{\rm d}n(M,z)}{{\rm d}M}A(M,F_{\rm sub.})\int {\rm d}M_s M_s^{-\beta} \\ &\times \int\limits_{r=0}^{r_{\rm vir.}(z,M_s)} \rho^2(r, c_{\rm vir.}^{\rm sub.}[M_s,z])4\pi r^2{\rm d}r. \end{aligned} \tag{37}$$

However as mentioned above, each subhalo is likely to itself host substructures with mass function

$$\frac{{\rm d}N}{{\rm d}M_{ss}} = A(M_s,F_{ss},\beta)M_s^{-\beta_{ss}}. \tag{38}$$

Owing to the self-similar nature of the mass distribution of substructures within halos, we take the values of the index β_{ss} and the sub-subhalo mass fraction per mass decade F_{ss} to be equal to β and $F_{\rm sub.}$ respectively. Hence, following the above treatment for halos and their subhalos, the clumping factor for all sub-subhalos with virial concentration $c_{\rm vir.}^{ss}$ residing within subhalos, themselves residing within halos located at redshift z is given by

$$\begin{aligned} C_{\rm sub-subhalos} &= 1 + \frac{(1+z)^3}{\bar\rho_{\rm DM}^2(z)}\int {\rm d}M\frac{{\rm d}n(M,z)}{{\rm d}M} \\ &\times A(M_s,F_s)\int {\rm d}M_s M_s^{-\beta} \\ &\times A(M_{ss},F_{ss})\int {\rm d}M_{ss} M_{ss}^{-\beta_{ss}} \\ &\times \int_{r=0}^{r_{\rm vir.}(z,M_s)} \rho^2(r, c_{\rm vir.}^{\rm ss}[M_{ss},z])4\pi r^2{\rm d}r. \end{aligned} \tag{39}$$

Finally, using equations (31), (37) and (39), we can now write down the total clumping factor for all structures at redshift z:

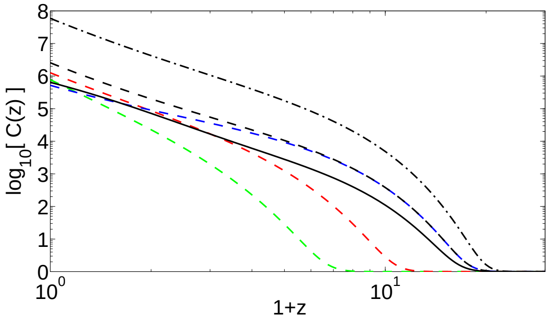

Figure 5. Plots of $C_{\rm total}(z)$ for structures with Burkert (solid black), NFW (dashed black) and Moore (dot-dashed black) density profiles for values of $(M_{\rm min.}/M_\odot, M_{\rm cut}/M_\odot) = (10^6, 10^6)$ with subhalo and sub-subhalo mass fractions per decade $F_{\rm sub}$ and $F_{\rm ss}$ of 0.3 and a relative concentration ratio N_c of 3.0. Also displayed are the corresponding values of $C_{\rm halo}(z), C_{\rm subhalos}(z)$ and $C_{\rm sub-subhalos}(z)$ associated with those structures with NFW profiles (dashed blue, red and green curves, respectively).

$$\begin{aligned} C_{\rm total} &= 1 + (C_{\rm halo}(z) - 1) \\ &+ (C_{\rm subhalos}(z) - 1) \\ &+ (C_{\rm sub-subhalos}(z) - 1), \end{aligned} \tag{40}$$

where we must modify the normalisation of expressions $C_{\rm halo}$ and $C_{\rm subhalos}$ to include the fact that a proportion of the mass of each halo and subhalo is provided by substructures. From the repetitive structure of equation (39), one can easily see how to extend the present scenario to include higher generations of substructures, but considering there is no evidence for such structures we do not include them in this study.

In figures (5), (6) and (7), we display the total clumping factor for various different scenarios in order to illustrate the relative ambiguity in its values associated with the varying levels of uncertainty on the various parameters involved. In addition in fig. (5) we illustrate the halo, subhalo and sub-subhalo contributions to the total clumping factor $C_{\rm total}(z)$ for structures possessing NFW density profiles. One can also see that the relative contribution to $C_{\rm total}(z)$ steadily descends for realistic values of the concentration ratio N_c and substructure fraction $F_{\rm sub}$ to the extent that further generations of substructures, if they exist, are unlikely to increase $C_{\rm total}(z)$ by more than a few percent, and hence we neglect their contribution here.

5 ABSORBED FRACTION OF INJECTED ENERGY

In order to compute the rate at which energy is injected into the IGM, we need to reliably estimate how much of the energy produced in the DM annihilations is actually transferred to the IGM, possibly altering its thermal/ionisation history. The energy absorbed fraction term $f_{\rm abs}$ in Eq. (1) thus denotes the fraction of the particle rest mass energy that is injected in the IGM at a given redshift. This depends on the spectrum of DM annihilation products and on their interaction with the IGM.

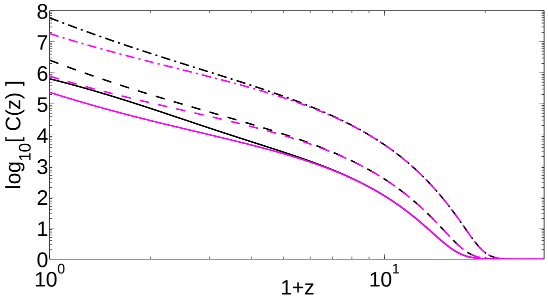

Figure 6. Plots of $C_{\rm total}(z)$ for structures with Burkert (solid), NFW (dashed) and Moore (dot-dashed) density profiles for values of $(M_{\rm min.}/M_\odot, M_{\rm cut}/M_\odot) = (10^6, 10^6)$ with subhalo and sub-subhalo mass fractions $F_{\rm sub}$ and $F_{\rm ss}$ of 10% and a relative concentration ratios N_c of 3.0 (black curves) and 1.5 (magenta curves).

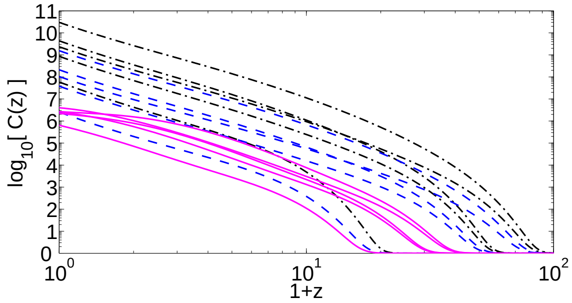

Figure 7. Plots of $C_{\rm total}(z)$ for structures with Burkert (magenta solid), NFW (blue dashed) and Moore (black dot-dashed) density profiles with subhalo and sub-subhalo mass fractions per decade $F_{\rm sub}$ and $F_{\rm ss}$ of 0.03, a relative concentration ratio N_c of 3.0, with values of $(M_{\rm min.}/M_\odot, M_{\rm cut}/M_\odot)$ equal to $(0.16, 0.16)$, $(0.16, 10^6)$, $(46, 46)$, $(46, 10^6)$ and $(10^6, 10^6)$ for the Burkert profile (respective descending curves at high-z), and $(10^{-12}, 10^{-12}), (10^{-12}, 10^6), (10^{-4}, 10^{-4}), (10^{-4}, 10^6)$ and $(10^6, 10^6)$ for NFW and Moore profiles (respective descending curves at high-z).

Neutralino dark matter can annihilate directly into either a fermion pair or weak gauge bosons. Since the cross section for annihilation to fermion pairs is proportional to the square of the final state fermion mass, this process will be dominated by heavy final states, namely $b\bar{b}$, $\tau^-\tau^+$ and $t\bar{t}$ (if kinematically allowed), while direct annihilation into electron-positron pairs will be strongly suppressed. Then we need to consider the following annihilation modes: $\chi\chi \to W^+W^-$, $\chi\chi \to ZZ$, $\chi\chi \to b\bar{b}$, $\chi\chi \to \tau^+\tau^-$,$\chi\chi \to t\bar{t}$. Both the gauge bosons and the fermion pairs produced in the neutralino annihilation will initiate a cascade that will eventually lead to a continuum of photons, neutrinos, electron/positrons pairs and protons final states, extending to energies much smaller than the rest mass of the DM particle. In Figs. 8 and 9 we show the photon and electron spectra dN/dE for different annihilation channels and for neutralino

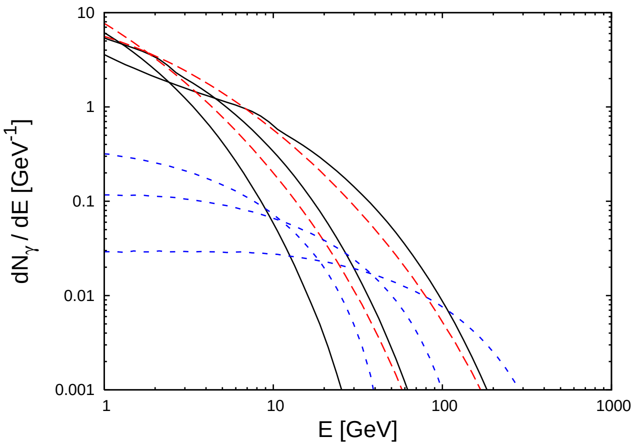

Figure 8. The photon spectrum from neutralino annihilation for different channels. The solid black lines represent the single annihilation spectrum for the channel $\chi\chi \rightarrow b\bar{b}$, for neutralino masses of 50, 150 and 600 GeV from left to right. The blue short-dashed lines are the same for the $\chi\chi \rightarrow \tau^+\tau^-$ channel. The red long dashed lines are for the $\chi\chi \rightarrow W^+W^-$ channel, for a neutralino mass of 150 and 600 GeV.

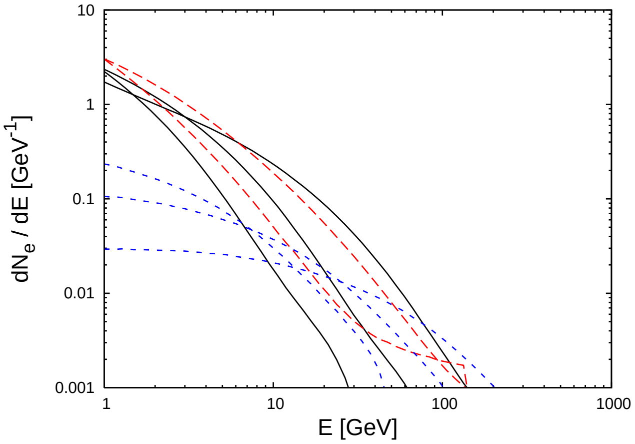

Figure 9. The electron spectrum from neutralino annihilation for different channels. The lines are the same as in Fig. 8.

masses of 50, 150 and 600 GeV. The spectra were calculated using PYTHIA[9] (Sjostrand et al. 2001).

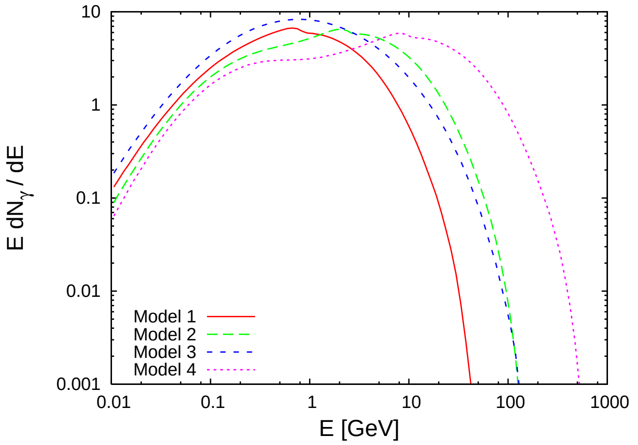

Figure 10. Photon energy spectrum EdN_γ/dE from neutralino annihilation, for the four models described in the text.

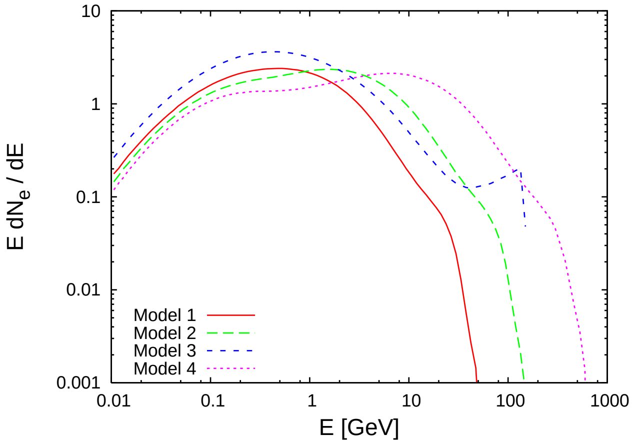

Figure 11. Electron energy spectrum EdN_e/dE from neutralino annihilation, for the four models described in the text.

The actual spectrum produced by the annihilations will depend on the branching ratios of the various channels; this in turn will be determined by the gaugino and higgsino fractions of the neutralino. In the following, we will consider four representative supersymmetry scenarios, in a similar way to what was done by Hooper et al. (2004). First we consider a 50 GeV neutralino with an annihilation branching ratio of 0.96 to $b\bar{b}$ and of 0.04 to $\tau^+\tau^-$ (designated as model 1). Such a particle could be gaugino-like or higgsino-like, since for masses below the gauge boson masses, these modes dominate for either case.

Second, we consider two cases for a 150 GeV neutralino. One (designated as model 2) which annihilates as described in model 1 , and another (designated as model 3) which annihillates entirely to gauge bosons, W^+W^- or ZZ . Such neutralinos are typically gaugino-like and higgsino-like respectively.

Finally we consider heavy, 600 GeV neutralinos, which annihilate to $b\bar{b}$ with a ratio of 0.87 and to $\tau^+\tau^-$ or t^+t^- the remaining time (designated as model 4).

In Figs. 10 and 11 we show spectrum of photons and electrons produced in a single annihilation, for these four neutralino models.

Although these models do not fully encompass the extensive parameter space available to neutralinos at present, they do describe effective MSSM benchmarks. Furthermore, the relevant results for neutralinos with a mixture of the properties of those above can be inferred by interpolating between those presented.

---

[9] http://home.thep.lu.se∼torbjorn/Pythia.html

We also consider a light dark matter candidate, annihilating directly into electron-positron pairs. This will result in a monochromatic spectrum with $E = m_{\rm DM}$. We consider two different LDM candidates with masses $m_{\rm DM} = 3,\ 20\,{\rm MeV}$ respectively.

The various final annihilation products have different interactions with the particles in the IGM. In the following we will examine the interaction of photons and pairs with the IGM. Protons are very penetrating and thus do not transfer energy to the IGM; neutrinos interactions are so weak that they are also unable to transfer energy to the IGM, so that the annihilation energy that ends up into protons and neutrinos is effectively lost for the purpose of heating/ionising the IGM.

5.1 Photons

In this paper we are mostly interested in the absorption of γ-ray photons. The absorption processes of x-ray and γ-ray photons at cosmological distances were discussed by Zdziarski & Svensson (1989). In principle, the possible energy loss mechanisms for photons are: photoionisation of atoms; Compton scattering on electrons; pair production on atoms; pair production of free electrons or nuclei; scattering on CMB photons; pair production on CMB photons. The total rate for fractional energy loss $\phi_\gamma(z,\,E)$, i.e., the fraction of the photon energy that is lost in a unit time, is given by a sum over the contributions of the single processes:

$$\phi_\gamma(z,\,E) = -\frac{1}{E}\frac{dE}{dt} = \sum_i \phi_{\gamma,i} \qquad (41)$$

where the index i runs over the different processes listed above. However, for $z \lesssim 500$, the dominant processes are photoionisation, effective for energies below ~ 10 keV, and pair production on CMB photons, effective for energies above $\sim 10 \div 100$ GeV. Compton scattering is effective only for $z \gtrsim 100$, in a range of photon energies roughly centered around ~ 1 MeV; at $z = 500$, the region where absorption is dominated by Compton scattering extends roughly from 10 keV to 30 MeV. The other processes, namely scattering on CMB photons and pair production on atoms, can be safely neglected for our purposes since they are only relevant at large redshifts.

The rate for fractional energy loss by photoionisation $\phi_{\gamma,\rm ion}$ is given by:

$$\phi_{\gamma,\rm ion}(z,E) = \frac{\sigma_{\rm He+H}(E)}{16} n_b(z)c, \qquad (42)$$

where $n_b(z)$ is the number density of baryons at redshift z, and $\sigma_{\rm He+H}$ is the absorption cross section per helium atom (hence the factor of 16 in Eq. 42, since $n_{\rm He} = n_b/16$), given by:

$$\sigma_{\rm He+H}(E) = 5.1\times10^{-20}\left(\frac{E}{250\,{\rm eV}}\right)^{-p}{\rm cm}^2, \qquad (43)$$

where $p = 3.3$ for $E > 250\,{\rm eV}$, $p = 2.65$ for $25 \leqslant E \leqslant 250\,{\rm eV}$.

The fractional energy loss rate by Compton scattering is:

$$\phi_{\gamma,\rm com}(z,E) = \sigma_T\,\epsilon\,g(\epsilon)n_e(z)c, \qquad (44)$$

where σ_T is the Thomson cross section, $\epsilon = E/m_ec^2$ is the photon energy in units of the electron mass, $n_e \simeq 0.88 n_b$ is the total electron density at redshift z (including both free and bound electrons), and $g(\epsilon)$ is:

$$g(\epsilon) = \frac{3}{8}\left[\frac{(\epsilon-3)(\epsilon+1)}{\epsilon^4}\ln(1+2\epsilon) + \frac{2\left(3+17\epsilon+31\epsilon^2+17\epsilon^3-10\epsilon^4/3\right)}{\epsilon^3(1+2\epsilon)^3}\right]. \qquad (45)$$

The pair production term is:

$$\phi_{\gamma,\rm pair}(z,E) = 2\pi^{1/2}\alpha^2\frac{c}{\lambda_c}\Theta^3 f(\epsilon\Theta) \qquad (46)$$

where α is the fine structure constant, λ_c is the Compton wavelength, $\Theta = kT_{cmb}/m_ec^2$ is the CMB temperature in units of the electron mass, and the function $f(x)$, in the limit $x \ll 1$, is given by:

$$f(x) = x^{-1/2}\exp\left(-\frac{1}{x}\right)\left(1+\frac{9}{4}x-\ldots\right). \qquad (47)$$

The condition $\epsilon\Theta \ll 1$ can be expressed as $E \ll 10^{15}\,{\rm eV}/(1+z)$, so this form of the cross section is adequate for our purposes.

In order to assess the efficiency of the energy loss mechanisms, the rate ϕ_γ should be compared with the expansion rate, as given by the value of the Hubble constant $H(z)$.When $\phi_\gamma \gg H(z)$, the photon loses all of its energy on a time scale small compared to the cosmological time, so that the energy loss mechanisms are very effective and the Universe is opaque to its propagation. It can then be assumed that all the photon energy is instantly deposited in the IGM. In the opposite regime, $\phi_\gamma \ll H(z)$, the photon loses a significant fraction of its energy on a time scale larger than the cosmological time, and the Universe is effectively transparent to the photon propagation.

This is illustrated in Fig. 12 where we show the photon transparency window in the $(E,\,z)$ plane. For illustrative purposes, we consider redshifts as large as $z = 1000$ in the figure, so that, in addition to the three processes for which we have listed explicitly the energy loss rates, we have also included the scattering over CMB photons and the pair production over nuclei in our computation of the total rate ϕ_γ. In the filled region, $\phi_\gamma > H(z)$, corresponding to the optically thick regime. In the white region, $\phi_\gamma < H(z)$, corresponding to the optically thin regime.

We will compute the absorbed fraction in detail in Sec. 5.3, however we can already gain some qualitative insight by looking at the figure. For the supersymmetric models considered, the average energy of the photons produced in the annihilation is of order of few GeVs, and in any case their energy is at most a few hundreds of GeVs (in the case of our heaviest candidate, the 600 GeV neutralino of model 4, only $\sim 1\%$ of the total energy produced in the annihilation is released in the form of photons with energy $E_\gamma > 200$ GeV). As it can be seen from the figure, this photons lie in the middle of the transparency window: their energy is too low for pair production, as already noticed, but on the other hand it is too high for photoionisation (or Compton scattering at $z > 100$) to be effective. These photons will propagate freely

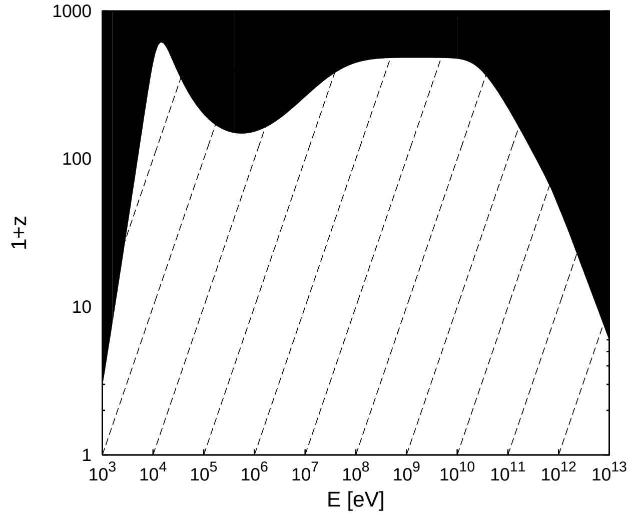

Figure 12. Photon transparency window. In the black region, the photon loses all of its energy through interaction with particle in the IGM and CMB photons. In the white region, the photon can propagate freely. The dashed lines represent photon trajectories.

and their energy will decrease due to the cosmological expansion. Although it is in principle possible that due to the cosmological redshift effect a photon produced in the transparency window at a given time will be absorbed later, we see from the figure that this is practically never the case. In conclusion we expect that the absorbed fraction for photon will be very small, and that the photons produced in neutralino annihilations will instead show up in the diffuse gamma background.

5.2 Electron-positron pairs

Electrons and positrons can lose energy through collisional ionisation of atoms or through inverse Compton scattering on CMB photons. In addition, positrons can annihilate with thermal electrons, but we have verified that this process is always subdominant with respect to inverse Compton scattering, and we will neglect it in the following. Other energy loss mechanisms, like synchrotron radiation loss, can also be safely neglected.

The rate for energy loss through collisional ionisation is:

$$\phi_{e,\mathrm{ion}}(E,z) = \frac{v}{E}\frac{2\pi e^4}{m_e v^2} \times \left\{ Z_{\mathrm{H}} n_{\mathrm{H}} \left[\ln\left(\frac{m_e v^2 \gamma^2 T_{\max,\mathrm{H}}}{2 I_{\mathrm{H}}^2} \right) + \mathcal{D}(\gamma) \right] + Z_{\mathrm{He}} n_{\mathrm{He}} \left[\ln\left(\frac{m_e v^2 \gamma^2 T_{\max,\mathrm{He}}}{2 I_{\mathrm{He}}^2} \right) + \mathcal{D}(\gamma) \right] \right\}, \quad (48)$$

where v is the electron velocity, $\gamma = E/m_e c^2$ is the electron Lorentz factor, $I_{\mathrm{H}} = 13.59\,\mathrm{eV}$ and $I_{\mathrm{He}} = 24.6\,\mathrm{eV}$ are the hydrogen and helium ionisation thresholds respectively, Z_{H} and Z_{He} are the hydrogen and helium atomic numbers, the function $\mathcal{D}(\gamma)$ is given by:

$$\mathcal{D}(\gamma) = \frac{1}{\gamma^2} - \left(\frac{2}{\gamma} - \frac{1}{\gamma^2} \right) \ln 2 + \frac{1}{8} \left(1 - \frac{1}{\gamma} \right)^2, \quad (49)$$

and $T_{\max,\mathrm{H}}$ and $T_{\max,\mathrm{He}}$ are the maximum energy transfers in a single collision:

$$T_{\max,\mathrm{H}} = \frac{2\gamma^2 m_{\mathrm{H}}^2 m_e v^2}{m_e^2 + m_{\mathrm{H}}^2 + 2\gamma m_e m_{\mathrm{H}}}, \quad (50)$$

$$T_{\max,\mathrm{He}} = \frac{2\gamma^2 m_{\mathrm{He}}^2 m_e v^2}{m_e^2 + m_{\mathrm{He}}^2 + 2\gamma m_e m_{\mathrm{He}}}. \quad (51)$$

The fractional energy loss rate through inverse Compton scattering is given by:

$$\phi_{e,\mathrm{com}}(z,E) = \frac{4}{3}\frac{\sigma_T c U_{\mathrm{CMB}}(z)}{m_e c^2}\frac{\gamma^2 - 1}{\gamma}, \quad (52)$$

where $U_{\mathrm{CMB}}(z)$ is the CMB energy density at redshift z.

In the case of inverse Comptons losses, it must be taken into account that the electrons and positrons do not transfer their energy directly into the IGM; instead, they accelerate the CMB photons, boosting their energy by a factor $\sim \gamma^2$. These up-scattered photons can either be absorbed by the IGM or escape, depending on their energy. As explained above, at redshifts below a few hundreds, the only relevant photon absorption processes are photoionisation, compton scattering and pair production. The latter is only efficient for photon energies below above (at least) $\sim$ 10 GeV; a simple calculation shows that the electrons and positrons produced in the annihilation of the dark matter candidates considered here are not energetic enough to boost the CMB photons above the threshold for pair production. We can also safely neglect compton scattering, since it is only efficient for $z > 100$ and in a small energy region around 1 MeV. Then we need to consider only photoionisation as the secondary process leading to the absorption of the photons produced by inverse compton scattering of electrons and positrons.

In order to modelize this effect, we proceed as follows. We consider that a scattered photon is absorbed through photoionisation if $\phi_{\gamma,\mathrm{ion}}(z,E) > H(z)$; this condition amounts to the requirement that the energy of the photon after the interaction should be smaller than

$$E_{\max,\mathrm{ion}}(z) = 0.64\,\mathrm{keV} \times \left[\left(\frac{\Omega_m h^2}{0.11} \right) \left(\frac{\Omega_b h^2}{0.0224} \right) (1+z)^{3/2} \right]^q, \quad (53)$$

where $q = 0.3$, and we have assumed a matter dominated Universe.

The energy density U'_{CMB} of photons that will be absorbed after the interaction, as a function of the electron Lorentz factor and of redshift, is then given by:

$$U'_{\mathrm{CMB}}(\gamma,z) = \frac{8\pi}{(hc)^3} \int_{E_{\min,\mathrm{ion}}/\gamma^2}^{E_{\max,\mathrm{ion}}/\gamma^2} \mathrm{d}E \frac{E^3}{\mathrm{e}^{E/kT_{\mathrm{CMB}}(z)} - 1}, \quad (54)$$

where the factors of γ^2 in the integration limits are due to the fact that the energy of the photon is increased by a factor of γ^2 after the interaction. The above expression can be recast as follows:

$$U'_{\mathrm{CMB}} = \frac{U_{\mathrm{CMB}}}{\pi^4/15} \int_{y_{\min}}^{y_{\max}} \frac{y^3}{\mathrm{e}^y - 1} dy, \quad (55)$$

where $y_{\min} \equiv E_{\min,\mathrm{ion}}/(\gamma^2 k T_{\mathrm{CMB}})$, and analogously for $y_{\max}$.

Finally, we can estimate the rate of energy injection into the IGM by inverse Compton $\Phi_{e,\mathrm{com}}(z,E)$ by replacing the total energy density U_{CMB} in Eq. (52) with the "reduced"

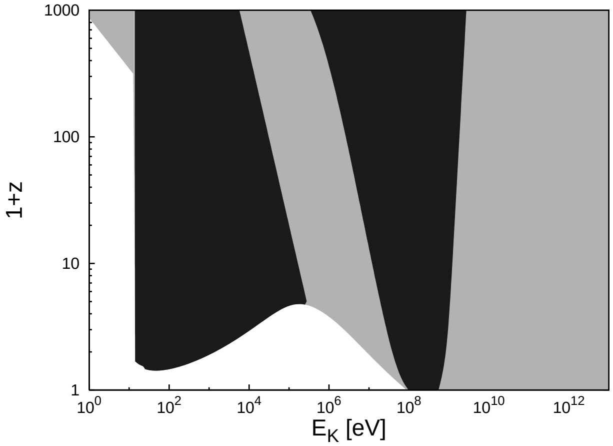

Figure 13. Transparency window for electrons. In the white region, electrons propagate freely. In the gray regions, electrons transfer all of their energy to the CMB photons, but these are subsequently lost, so that no energy is injected in the IGM. In the black regions, all the electron energy is efficiently injected in the IGM. See text for discussion.

energy density $U'_{\rm CMB}$. This amounts to weighting the inverse compton absorption rate $\phi_{e,\rm com}$ by an efficiency factor $\eta \equiv U'_{\rm CMB}/U_{\rm CMB}$:

$$\Phi_{e,\rm com}(z,E) = \eta(z,E)\,\phi_{e,\rm com}(z,E). \qquad (56)$$

The behaviour of electron-positron pairs with respect to the energy transfer to the IGM is summarized in Fig. 13. In the white region, the total energy loss rate is smaller than the expansion rate: $\phi_{e,\rm ion} + \phi_{e,\rm com} < H$, so that Universe is transparent to the propagation of electrons. In the grey regions, the electrons and positrons interact by inverse Compton scattering, but the resulting photons fall in the photon transparency window. This means that the Universe is opaque to the propagation of electrons, but nevertheless their energy is not transferred to the IGM. This corresponds to the regime in which $\phi_{e,\rm com} > H$, $\phi_{e,\rm ion}$ but $\Phi_{e,\rm com} < H$. Finally, in the black regions the electron energy is efficiently transferred to the intergalactic medium. In particular, the region on the left correspond to the case in which $\phi_{e,\rm ion} > H$, $\phi_{e,\rm com}$, meaning that collisional ionisation is the dominant process; the region on the right correspond to $\phi_{e,\rm com} > H$, $\phi_{e,\rm ion}$ and $\Phi_{e,\rm com} > H$, meaning that inverse Compton is the dominant interaction, and that the upscattered CMB photons fall into the photon absorption window.

5.3 Energy absorbed fraction

The energy deposition of photons and pairs in the IGM has been worked in detail by Ripamonti, Mapelli & Ferrara (2007). Here we will consider a more simplified approach, in the form of a "on the spot" approximation. In practice, we will be comparing the energy loss rate ϕ of the product particle, for example a photon, with the cosmological expansion rate H. If $\phi > H$, we consider that all the energy of the particle is immediately absorbed by the IGM; if on the contrary $\phi < H$, we consider that the particle energy is "lost" for the purpose of heating the IGM. In the case of electrons and positrons losing energy via inverse Compton scattering with the CMB photons, we take into account the efficiency related to the transfer of energy from the scattered photons to the IGM, as explained in the previous section.

In more detail, what we do is the following. At every redshift, starting from $z = 500$, we compute the absorption region $\mathcal{A}_i(z)$ for every kind of particle, i.e., the energy range in which particles of that kind efficiently transfer their energy to the IGM, using the $\phi \lessgtr H$ criterium. We note that the region $\mathcal{A}_i$ will possibly consist of two or more disconnected intervals. For example, by looking at Fig. 13 we see that for electrons the region $\mathcal{A}_e(z = 100)$ is roughly the union of the two intervals $10\,\mathrm{eV} \leqslant E_K \leqslant 100\,\mathrm{keV}$ and $10\,\mathrm{MeV} \leqslant E_K \leqslant 1\,\mathrm{GeV}$, E_K being the kinetic energy of the electron.

Then we evaluate the energy absorbed fraction simply as the ratio of the energy that is absorbed to the total energy produced in the annihilation,:

$$f_{\rm abs}(z) = \frac{\displaystyle\sum_i \int_{\mathcal{A}_i(z)} E\frac{dN_i(E)}{dE}dE}{2m_{dm}c^2} \qquad (57)$$

where the sum runs over the different annihilation products. For electrons and positrons, in the region where inverse compton scattering is the dominant loss mechanism, we additionaly weight the integrand in Eq. (57) with the efficiency factor η defined in the previous section, in order to account for the finite fraction of the energy lost by the electron that is actually injected into the IGM.

In Fig. 14 we show the energy absorbed fraction for the supersymmetric models described at the beginning of this section. We see that for all four models, $f_{\rm abs}$ is nearly constant and always much smaller than unity at the redshifts of interests. In particular, $f_{\rm abs}$ goes from $\sim 10^{-2}$ for the model with the lightest candidate (model 1, $m_\chi = 50\,\mathrm{GeV}$) to $\sim 10^{-4}$ for the model with the heaviest candidate (model 4, $m_\chi = 600\,\mathrm{GeV}$). This behaviour can be understood as follows. The photons and electrons produced in neutralino annihilations peak at $E \sim 1\,\mathrm{GeV}$ for models 1 to 3, and at $E \sim 10$, GeV for model 4. Thus photons are in the middle of the transparency window and do not get absorbed. Electrons (and positrons), on the other hand, possibly lie in (or close to) the region in which energy is transferred to the IGM by means of inverse Compton scattering over CMB photons and the subsequent absorption of those through photoionisation. This region is roughly centered around $E \sim 0.1\,\mathrm{GeV}$ so that lighter neutralinos, producing softer annihilation spectra, will be absorbed more easily. This also explains while model 3 neutralinos inject more energy than their model 2 counterparts: the neutralino mass is the same in both models, both the former produces sligthly less energetic electrons.

In Fig. 15 we show the energy absorbed fraction for the two LDM models considered. In this case we see that the energy absorbed fraction is larger with respect to the SUSY scenarios. For the lightest candidate, $m_{LDM} = 3$, GeV, the energy absorbed fraction is 1 at $z = 1000$, then decreases quite rapidly, reaching a minimum value $f_{\rm abs} \simeq 5 \times 10^{-2}$ at redshift 100, and again starts to increase slowly. In the case

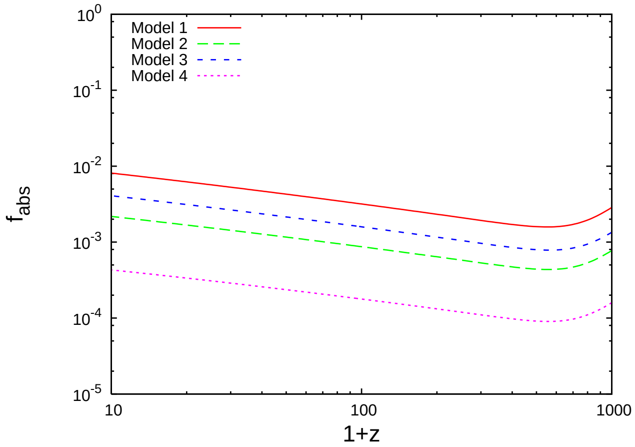

Figure 14. Energy absorbed fraction $f_{\rm abs}$ for the four neutralino models described in the text. The red solid line is for a 50 GeV neutralino. The green long-dashed line is for a 150 GeV, gaugino-like neutralino. The blue short dashed line is for a 150 GeV, higgsino-like neutralino. The magenta dotted line is for a 600 GeV, gaugino-like neutralino. A smaller neutralino mass leads to a larger absorption. See text for discussion.

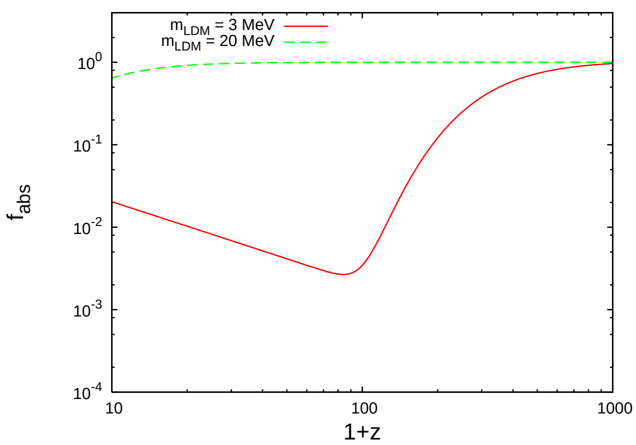

Figure 15. Energy absorbed fraction $f_{\rm abs}$ for the two LDM models described in the text. The red solid line is for a 3 MeV LDM particle. The green long-dashed line is for a 20 MeV LDM particle. A larger particle mass leads to a larger absorption. See text for discussion.

of the heaviest candidate, $m_{LDM} = 20\,$GeV, the absorbed fraction stays constant and equal to 1 until $z \sim 10$, where it starts to decrease. This behaviour can also be understood in terms of the transparency/absorption windows studied in the previous section. We considered LDM decaying directly to electron-positron pairs only, so that every particle produced carries an energy equal to the DM particle mass. As it can be seen from Fig. 13, a 3MeV electron lies in the absorption region only if it is produced at redshifts close to 1000. Electrons produced later lie outside this region, and this explains why $f_{\rm abs}$ decreases between $z = 1000$ and $z = 100$. The increase after $z = 100$ is due to the increased importance of collisional ionisation (the ratio $\phi_{\rm e,ion}/H$ scales with redshift like $(1+z)^{3/2}$). On the other hand, 20 MeV electrons always lie in the absorption region from $z = 1000$ to $z = 10$, and only after that they fall ouside it; this is why the absorbed fraction is always $\simeq 1$ in this redshift range.

In the derivation above we have implicitly assumed that the Universe is mostly neutral in the redshift range of interest. When the Universe starts to be reionised, the energy loss rate for photoionisation will become smaller, since it is proportional to the density of neutral atoms. From the discussion above, we have seen that the energy produced in DM annihilations is mainly injected into the IGM through inverse Compton scattering over CMB photons ($e\gamma_{\rm CMB} \rightarrow e\gamma$) followed by absorption of the photon via photoionisation ($\gamma A \rightarrow A^+ e^-$). Then we expect the absorbed fraction to start going rapidly to zero once reionisation begins, at $z \sim 10$.

6 THE 21 CM BACKGROUND

The emission or absorption of the 21cm line signal emanating from neutral gas is associated with the transition between the $n = 1$ triplet and singlet hyperfine levels of hydrogen. The transition rate is governed by the spin temperature, T_s, defined as

$$\frac{n_1}{n_0} = 3\exp\left(\frac{-T_*}{T_s}\right), \qquad (58)$$

where n_0 and n_1 are the respective number densities of hydrogen atoms in the singlet and triplet states, and $T_* = 0.068$K is the equivalent temperature corresponding to the transition energy.

6.1 CMB - kinetic temperature coupling

In the presence of the CMB radiation field, the spin temperature of the neutral hydrogen gas rapidly tends towards the CMB temperature $T_{\rm CMB} \simeq 2.725(1+z)$K. In order for neutral hydrogen gas to produce a detectable signal in the 21cm background, be it absorption or emission, that is distinguishable from that generated from the CMB, the kinetic temperature T_K of the gas must decouple from $T_{\rm CMB}$.

In a Universe containing stable, non-annihilating dark matter, the spin temperature and the kinetic temperature of HI gas are coupled to the $T_{\rm CMB}$ until $z \simeq 200$. At $30 \lesssim z \lesssim 200$, prior to the formation of non-linear baryonic structures, the IGM cools adiabatically, i.e. $T_K \propto (1+z)^2$, compared to $T_{\rm CMB} \propto (1+z)$. During this epoch spin-exchange collisions between hydrogen atoms, protons and electrons are efficient at coupling T_K and T_S of the gas, and consequently an absorption at wavelength $\lambda = 21(1+z)$ cm can be observed until approximately $z \simeq 70$. At later times cosmological expansion reduces the frequency of these collisions significantly to the extent where T_S re-couples with $T_{\rm CMB}$, diminishing the 21 cm absorption signal.

However, in a Universe containing annihilating/decaying dark matter which injects an appreciable of energy into the IGM, the thermal history of the gas may be significantly altered to the extent where the corresponding changes in the evolution of the 21 cm signal are detectable by current and future radio interferometers. Of particular importance is the high sensitivity of these changes with respect to the nature of the dark matter, making them a powerful tool for constraining the properties of potential dark matter candidates.

There are two mechanisms which can decouple T_S from $T_{\rm CMB}$: firstly, the fore-mentioned spin-exchange collisions between neutral atoms, electrons and protons, which are effective at $z \geqslant 70$ before the Hubble expansion has rarefied the gas in the IGM, and secondly, scattering by Lyman-α radiation ("Wouthuysen-Field" effect, also known as "Lyman-α pumping" (Wouthuysen 1952; Field 1959; Hirata 2006)), which couples T_S to T_K via the mixing of the $n=1$ hyperfine states through intermediate transitions to the $2p$ state.

In the quasi-static approximation for the population of the hyperfine levels in question, and in the absence of radio sources, the HI spin temperature is a weighted mean involving T_K and $T_{\rm CMB}$,

$$T_S = \frac{T_{\rm CMB} + yT_K}{1+y}, \tag{59}$$

The coupling coefficient y can be written as

$$y = y_\alpha + y_C, \tag{60}$$

where y_α is the term associated with Lyman-α pumping, given by

$$y_\alpha = \frac{P_{10} T_*}{A_{10} T_K}, \tag{61}$$

whilst y_C is associated with the de-excitation of the HI hyperfine triplet state due to collisions with neutral atoms, electrons and protons, collectively written as

$$y_C = \frac{T_*}{A_{10} T_K}(C_{\rm H} + C_e + C_p). \tag{62}$$

In the above equations $A_{10} = 2.85 \times 10^{-15}$s is the rate of spontaneous photon emission, P_{10} is the de-excitation rate of the hyperfine triplet state due to Lyman-α scattering and $C_{\rm H}, C_e$ and C_p are the de-excitation rates associated with collisions of hydrogen atoms with other hydrogen atoms, electrons and protons respectively. We write $P_{10} = (16\pi J_\alpha \sigma_\alpha)/(27 h_p \nu_\alpha)$, where J_α is the background intensity of Lyman-α photons, σ_α is the Lyman-α photon absorption cross-section for neutral hydrogen and $h_p = 6$ is Planck's constant. We neglect the small corrections to the above expressions proposed by Hirata (2006)). The H-H collision term can be written as $C_{\rm H} = k_{10} n_{\rm HI}$, where k_{10} is the effective single-atom collision rate coefficient for which we adopt the fit $k_{10} = 3.1 \times 10^{-11} T_K^{0.357} \exp(-32/T_K)$ cm^{3}s^{-1} proposed by Kuhlen et al. (2005), which is accurate to within 0.5% in the range $10 < T_K < 10^3$ K. For the e-H collision term, $C_e = n_e \gamma_e$, we have used the following fit proposed by Liszt (2001), $\log(\gamma_e/{\rm cm}^3{\rm s}^{-1}) = -9.607 + 0.5\log(T_K)\exp\left[-(\log T_K)^{4.5}/1800\right]$ for $1 < T_K < 10^4$K, $\log(\gamma_e/{\rm cm}^3{\rm s}^{-1}) = -9.607 + 0.5\log(T_K)$ for $T_K < 1$K (Smith 1966), and $\gamma_e(T_K > 10^4{\rm K}) = \gamma_e(10^4{\rm K})$. We ignore de-excitations involving collisions with protons since they are typically much weaker than those involving electrons at the same temperature.

6.2 Modifications to IGM thermal evolution when incorporating DM

In this section we describe the modifications to the standard equations describing thermal and ionisation history of the IGM when we incorporate the potentially significant energy deposition of the products of annihilating dark matter, which in turn determines the 21 cm signal.

We parameterize the effect of dark matter annihilation by the rate of energy injection given by eq. (1). This energy is then used to excite and ionise the hydrogen and helium atoms in the IGM. We will not enter in the detail of the partition of energy between hydrogen and helium, but instead assume that it is divided proportionally to the respective number densities. This means that a fraction $1/(1+f_{\rm He})$ of the absorbed energy will go to hydrogen, while a fraction $f_{\rm He}/(1+f_{\rm He})$ will go to helium, $f_{\rm He}$ being the helium to hydrogen number ratio. Then we need to know how the energy is partitioned between the different processes. The relative fractions χ_i, χ_h and χ_e of the energy absorbed which is diverted towards ionising, heating and exciting hydrogen and helium atoms were calculated by Shull & van Steenberg (1985). Their results can be approximated by (Chen & Kamionkowski 2004)

$$\chi_{i,j}(z) \sim \frac{[1 - x_j(z)]}{3} \tag{63}$$

$$\chi_{h,j}(z) \sim \frac{[1 + 2x_j(z)]}{3} \tag{64}$$

$$\chi_{e,j}(z) \sim \frac{[1 - x_j(z)]}{3} \tag{65}$$

where $x_j(z)$ is the ionisation fraction of the relevant nuclear species j (i.e. j=H or He for hydrogen or helium nuclei respectively), defined as

$$x_j = \frac{n_{j^+}}{n_j}, \tag{66}$$

where n_{j+} is the number density of ionised nuclei of the species j. We can also define a total ionisation efficiency $\chi_i \equiv (\chi_{i,\rm H} + f_{\rm He}\chi_{i,\rm He})/(1+f_{\rm He})$, and similar quantities for heating and excitation.

We compute ionisation and thermal history of the IGM when incorporating our chosen species of dark matter using the publicly available code RECFAST (Seager, Sasselov & Scott 1999, 2000), modifying the standard evolution equations for the ionisation fractions of hydrogen and helium nuclei, aswell as the evolution equation for the kinetic temperature as follows (Padmanabhan & Finkbeiner 2005),

$$-\delta\left(\frac{{\rm d}x[{\rm H}]}{{\rm d}z}\right) = \frac{\dot\epsilon}{I_H}\frac{\chi_{i,\rm H}}{(1+f_{\rm He})}\frac{1}{H(z)(1+z)}, \tag{67}$$

$$-\delta\left(\frac{{\rm d}x[{\rm He}]}{{\rm d}z}\right) = \frac{\dot\epsilon}{I_{\rm He}}\frac{\chi_{i,\rm He}}{(1+f_{\rm He})}\frac{1}{H(z)(1+z)}, \tag{68}$$

$$-\delta\left(\frac{{\rm d}T_k}{{\rm d}z}\right) = \frac{2\dot\epsilon}{3k_{\rm B}}\frac{(\chi_{h,\rm H} + f_{\rm He}\chi_{h,\rm He})}{(1+f_{\rm He})H(z)(1+z)}. \tag{69}$$

A further equation needed to calculate the 21 cm signal is that describing the evolution of the Lyman-α background intensity J_α, which can couple the spin and kinetic temperatures of the H-atoms in the IGM through the

Wouthuysen-Field effect. H-atoms, excited by collisions with fast photoelectrons subsequently produce a cascade of line photons, including Lyman-α photons which are then likely to be re-absorbed by the optically-thick IGM. We utilise the approximation adopted by Furlanetto et al. (2006) that approximately half of the total energy which is diverted to excite hydrogen is used to produce Lyman-α photons, i.e. $\chi_\alpha \sim \chi_{e,\mathrm{H}}/2$.

Following the treatment by Valdés et al. (2007) we obtain (however, please note the additional factor of ν_α in front of the expression)

$$J_\alpha = \frac{n_{\mathrm{H}}^2 hc\nu_\alpha}{4\pi H(z)}\left[x_e x_{e,\mathrm{H}}\alpha^{\mathrm{eff.}}_{2^2P} + x_{e,\mathrm{H}} x_{\mathrm{HI}}\gamma_{e\mathrm{H}} + \frac{\chi_\alpha \dot{\epsilon}}{n_{\mathrm{H}} h\nu_\alpha}\right], \quad (70)$$

where the first two terms are the contributions are associated with the collisional excitation involving electrons discussed above, and the last term is the contribution from dark matter. Also, $\alpha^{\mathrm{eff.}}_{2^2P}$ is the effective recombination coefficient to the 2^2P level (Pengelly 1964), and $\gamma_{e\mathrm{H}} \simeq 2.2\times10^{-8}\exp\left[-11.84/(T/10^4\,\mathrm{K})\right]\mathrm{cm}^3\mathrm{s}^{-1}$ is the collisional excitation rate of HI atoms involving electrons (Shull & van Steenberg 1985).

The quantity most intimately associated with the observations of the cosmological 21 cm signal intensity is the differential brightness temperature deviation, δT_b, between the 21 cm signal and the CMB, approximately given by (Field 1958, 1959; Ciardi & Madau 2003)

$$\begin{aligned}\delta T_b \quad &\simeq \quad 26\ \mathrm{mK}\ x_{\mathrm{HI}}\left(1-\frac{T_{\mathrm{CMB}}}{T_S}\right)\left(\frac{\Omega_b h^2}{0.02}\right)\\ &\times \quad \left[\left(\frac{1+z}{10}\right)\left(\frac{0.3}{\Omega_{\mathrm{M}}}\right)\right]^{1/2}, \qquad (71)\end{aligned}$$

where $x_{\mathrm{HI}} = 1 - x_{\mathrm{H}}$ is the averaged fraction of neutral hydrogen in the patch of sky being observed.

7 RESULTS

In the following section we illustrate our predictions for the effects on the thermal history of the IGM caused by the additional energy injected into it by annihilating neutralino and light dark matter, when including the effect of the enhancement from dark matter structures.

Since, as we have seen, this enhancement can be very large, boosting the DM annihilation rate by several orders of magnitude, we want to be sure that this does not spoil other observations. Then we perform two tests on each of the clumping factors investigated, before taking it into consideration for the purpose of its effect on 21cm observations. First of all, we check that the huge injection of energy into the IGM does not lead to a early ionisation. We use to this purpose our modified version of the RECFAST code described before, and discard all the clumping factors for which the ionised fraction $x_e > 0.01$ at $z = 14$. We choose this value of the redshift because it is close to the 2σ upper limit to z_{reion} coming from WMAP5 observations (Dunkley et al. 2008). Secondly, we check that the diffuse photon flux produced does not exceed observed diffuse background (adopting the conservative approximation that $f_{\mathrm{abs}} \sim 0$, that for all the models we consider is quite a good approximation at the present time $z = 0$, where the clumping factor reaches its maximum value). We use to this purpose the measurements of the diffuse gamma-ray background in the 1 MeV - 100 GeV range conducted by EGRET (Sreekumar et al. 1998; Strong, Moskalenko & Reimer 2004) and COMPTEL (Weidenspointner et al. 2000), and those of the diffuse X-ray background in the sub-MeV range conducted by the SPI spectrometer aboard INTEGRAL(Churazov et al. 2007).

In the following, owing to the fact that the effects on the spin and brightness temperature can be very subtle, we display results only for the the most optimistic clumping factors that conform to the above criteria. For reference, in the appendix to this paper we have tabulated the relevant astrophysical parameters associated with all clumping factors investigated, indicating which have been excluded on the basis of the criteria described above.

7.1 Neutralino dark matter

We begin with an analysis of neutralino dark matter. Whilst in all four of the models considered the deviations of the spin temperature from that calculated in a scenario where dark matter is excluded is marginal, there are significant deviations in the evolution of the kinetic temperature which we highlight below.

We start with model 1, a 50 GeV neutralino with a substantial Higgsino and Gaugino fraction that annihilates to $b\bar{b}$ pairs 96% of the time and to $\tau^+\tau^-$ otherwise, with a canonical annihilation cross-section of $\langle\sigma_{\mathrm{ann.}}v\rangle = 3\times10^{-27}/\Omega_{\mathrm{DM},0}h^2 \simeq 2.7\times10^{-26}\mathrm{cm}^3\mathrm{s}^{-1}$. Owing in particular to the very light nature of this neutralino, the energy injection rate is very large (since overall, $\dot{\epsilon}_{\mathrm{DM}}$ scales as m_{DM}^{-1}). Consequently, the majority of the clumping factors calculated using the Moore profile are excluded owing to the overproduction of gamma-rays. In figure 16 we display the effects of such dark matter particles on the evolution of the T_K and T_S (dot-dashed and dashed curves respectively) for the most optimistic clumping factors consistent with observations of the diffuse background, namely M18 (blue) and N4 (magenta) calculated using Moore and NFW density profiles respectively, compared to a scenario where dark matter is absent (black dot-dashed and black solid curves respectively). As can be seen from figure 16, significant heating of the IGM by dark matter begins when the respective clumping factors start to elevate significantly above unity, which for M18 corresponds to $z = 20$ and $z = 90$ for N4, indicating approximately when the lightest dark matter structures start to form.

Next we consider dark matter composed of neutralinos described by model 2, that is, 150 GeV Gaugino-dominated neutralinos, that annihilate 96% to $b\bar{b}$ and 4% to $\tau^+\tau^-$. Once again, the majority of the clumping factors calculated using the Moore profile are excluded owing to the overproduction of gamma-rays, with M8 being the most optimistic non-excluded clumping factor, whilst for structures with NFW profiles all but N1, N5 and N9 are permitted, with N2 being the most optimistic. In figure 17 we display the effects of such dark matter particles on the evolution of the T_K and T_S (dot-dashed and dashed curves respectively) for the clumping factors M8 (blue) and N2 (magenta) calculated using Moore and NFW density profiles respectively. From fig-

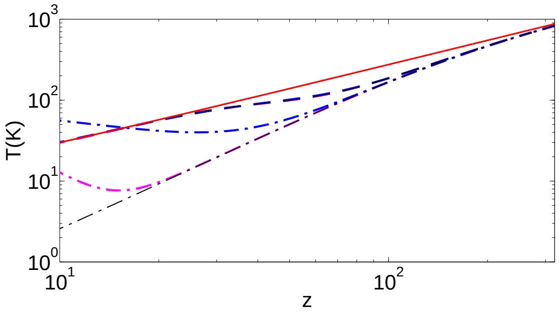

Figure 16. The evolution of the IGM kinetic and spin temperature (dot-dashed and dashed curves respectively) for the clumping factors M18 (blue) and N4 (magenta) calculated using Moore and NFW density profiles respectively, for structures composed of 50 GeV neutralino dark matter described by model 1 with annihilation cross-section $\langle\sigma_{\mathrm{ann.}}v\rangle = 2.7\times10^{-26}\mathrm{cm}^3\mathrm{s}^{-1}$, compared to a scenario with no dark matter (black dot-dashed and black dashed curves respectively). Also displayed is the temperature of the CMB (red solid curve).

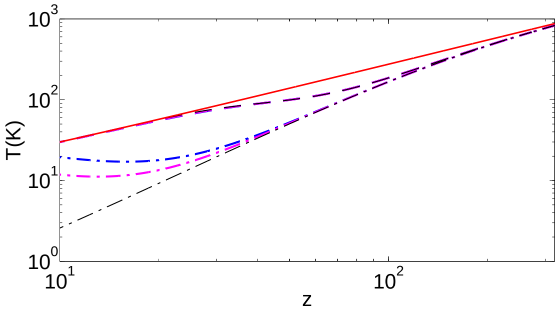

Figure 17. Same as for figure 16, but for dark matter composed of 150 GeV Gaugino-dominated neutralinos described by model 2 and using clumping factors M8 (blue) and N2 (magenta).

ure 17, the additional heating of the IGM by dark matter begins at similar times for both profiles, at around $z = 40$, although both M18 and N2 start to elevate significantly above unity at around $z = 100$. At all except recent times M8 is greater than N2 explaining the consistently increasing rate of T_K for M8 relative to that for N2.

Next we consider dark matter composed of neutralinos described by model 3, that is, 150 GeV Higgsino-dominated neutralinos, that annihilate 58% to W^+W^- and 42% to ZZ. One would expect that since the results associated with such dark matter to be very similar to that for neutralino dark matter described by model 2 since the energy injection rate is largely set by the dark matter particle mass m_χ. However, clumping factors M7 and M14 for structures possessing Moore profiles and N5 for NFW profiles are now permitted, because the annihilation products resulting from model 3 neutralinos produce an overall lower flux in photons. In figure 18 we display the effects of model 3 neutralino dark matter on the evolution of the T_K and T_S (dot-dashed and dashed curves respectively) for the clumping factors M7 (blue) and N2 (magenta). The similarity of these effects compared to the 150 GeV Gaugino-dominated neutralinos described by model 2 reaffirms the notion that it is the largely the neutralino mass that dictates the resulting deviations in the 21 cm signal rather than its Gaugino fraction. This result is not altogether surprising if one recognizes that the majority of the energy injected into the IGM by neutralinos ultimately ends up as electrons, positrons and photons regardless of the initial annihilation modes to the extent where these various subtleties between different types of neutralino are largely lost in the evolution of the T_K and T_S.

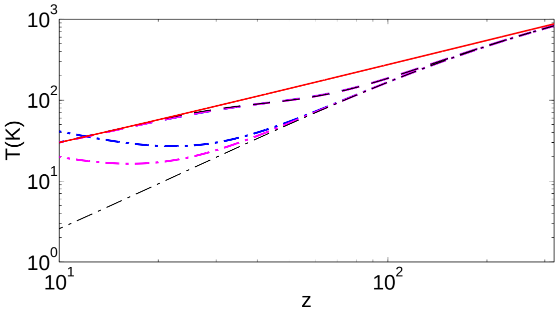

Figure 18. Same as for figure 16, but for dark matter composed of 150 GeV Higgsino-dominated neutralinos described by model 3 and using clumping factors M7 (blue) and N2 (magenta).

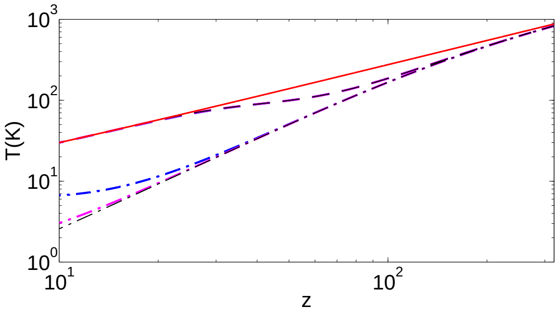

Figure 19. Same as for figure 16, but for dark matter composed of 600 GeV Gaugino-dominated neutralinos described by model 4 and using clumping factors M4 (blue) and N2 (magenta).

Finally, for dark matter composed of neutralinos described by model 4, that is, 600 GeV Gaugino-dominated neutralinos that annihilate 87% to $b\bar{b}$ and 13% to $\tau^+\tau^-$. In figure 19 we display the effects of model 4 neutralino dark matter on the evolution of the T_K and T_S (dot-dashed and dashed curves respectively) for the clumping factors M4 (blue) and N2 (magenta). All deviations from the “no dm” scenario are extremely suppressed even for the most optimistic clumping factors, which in this case are M4 and N2, for structures possessing Moore and NFW profiles respectively. This is due to the extremely suppressed energy injection rates arising from the large mass of the neutralino, relative to other neutralinos possessing similar clumping factors, with T_K only beginning to deviate from the “no dark matter” model at recent times when the clumping factors are largest.

7.2 Light dark matter

We now turn our attention to LDM. We consider two models, firstly dark matter composed of 3 MeV LDM par-

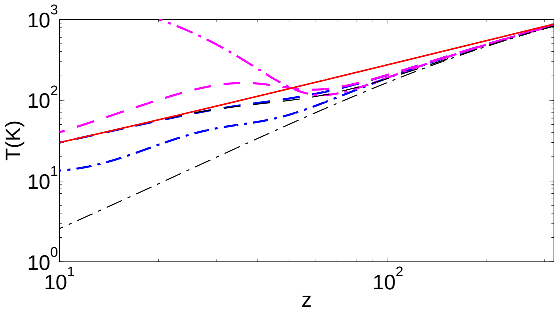

Figure 20. The evolution of the IGM kinetic and spin temperature (dot-dashed and dashed curves respectively) for 3 MeV (blue) LDM particles using the clumping factor B12 and an annihilation cross-section $\langle\sigma v\rangle = 1.29 \times 10^{-29}\mathrm{cm}^3\mathrm{s}^{-1}$, and also for 20 MeV (magenta) LDM particles using the clumping factor B7 and an annihilation cross-section $\langle\sigma v\rangle = 8.60 \times 10^{-29}\mathrm{cm}^3\mathrm{s}^{-1}$. The results for the evolution of the kinetic and spin temperature are compared to a those calculated when dark matter is absent (black dot-dashed and black dashed curves respectively). Also displayed is the temperature of the CMB (solid red curve).

ticles with an annihilation cross-section $\langle\sigma v\rangle = 1.29 \times 10^{-29}\mathrm{cm}^3\mathrm{s}^{-1}$, and secondly dark matter composed of 20 MeV LDM particles with an annihilation cross-section of $\langle\sigma v\rangle = 8.60 \times 10^{-29}\mathrm{cm}^3\mathrm{s}^{-1}$.

In figure 20 we display the effects of these dark matter candidates on the evolution of the kinetic and spin temperature of the IGM (dot-dashed and dashed curves respectively for 3 MeV (blue) and 20 MeV (magenta) LDM particles). Once again, for each model we use the most optimistic clumping factors consistent with observations of the diffuse background. For 3 MeV particles this corresponds to B12, calculated using a Burkert density profile. For 20 MeV particles the absorbed fraction, f_{abs}, of energy injected into the IGM is significantly larger than for the lighter candidate, allowing for larger enhancements to its rate of annihilation by dark matter over-densities, with B7 being the most optimistic clumping factor permitted.

As can be seen from figure 20, there is a marked difference in the effects of the two models. Both the 3 MeV and 20 MeV LDM models significantly heat the IGM at early times, resulting in T_K decoupling from its standard adiabatic revolution following the formation of the first structures, which corresponds to 10^6 $M_\odot$ halos at $z \simeq 50$, and 46 $M_\odot$ at $z \simeq 40$ respectively. For 3 MeV LDM this produces only modest changes in T_S relative to the standard case, slightly reducing the absorption signature approximately in the range $50 < z < 100$. However for 20 MeV LDM the larger clumping factor and absorbed fraction results in increasingly larger T_K to the extent where T_S exceeds T_{CMB} at $z \simeq 50$, resulting in an subsequent emission signature for the 21 cm signal that is still significant at $z = 10$.

7.3 The 21 cm global signature

Using the above results for the evolution of T_S, calculated for our neutralino and LDM candidates, we now calculate the evolution of the differential brightness temperature δT_b associated with the cosmological 21 cm signal , which is to be directly measured by radio interferometers such as LOFAR (see e.g. Best (2008)).

In figure 21 we display our results for the predicted evolution of δT_b for dark matter composed of annihilating LDM particles of mass 3 MeV (blue dashed) and 20 MeV (magenta dashed) relative to the standard scenario where dark matter is absent (black solid). For clarity, we neglected to superimpose results for δT_b associated with neutralino dark matter on the same axes owing to the very small deviations of these results from the standard case $\delta T_{b,0}$, relative to those obtained for LDM. However, in figure 22 we have displayed results for the deviations $\delta T_b - \delta T_{b,0}$ for neutralino dark matter, and again for LDM displayed separately in figure 23.

Firstly considering neutralino dark matter, the evolution δT_b is rather similar for all four models, differing approximately only in an overall normalisation resulting from competing effects involving a relative enhancement/suppression owing smaller/larger particle masses and larger/smaller clumping factor. As mentioned above, values of the brightness temperature deviation $|\delta T_b - \delta T_{b,0}|$ relative to the standard scenario remain very modest, with maximum values of $\leqslant (2-3)$ mK, at the two characteristic peaks occurring at $z \simeq 50-70$ and $z \simeq 20-30$. However, at $z \simeq 10$, such deviations are significantly reduced in all cases to less than 0.5 mK.

For LDM, the situation is far more interesting than for neutralino dark matter, since values of the brightness temperature deviation are far more significant. The evolution of δT_b is almost identical for both LDM for $z > 100$, with deviation from the standard case increasing up to $\simeq 15$ mK as the energy injected into the IGM by LDM annihilations forces δT_b to -30 mK at $z = 100$, compared to -50 mK when dark matter is absent. Subsequently, the rapidly decreasing value of $f_{\mathrm{abs.}}$ for 3 MeV particles results in a steadily decreasing value of $|\delta T_b - \delta T_{b,0}|$, reaching zero at $z \simeq 30$ and despite a slight increase in its subsequent evolution, $|\delta T_b - \delta T_{b,0}|$ returns to almost zero at $z = 10$. However, for 20 MeV LDM particles, $f_{\mathrm{abs.}}$ maintains its large value until much later times resulting in the continued increase in $\delta T_b - \delta T_{b,0}$ beyond $z = 100$, reaching a maximum of $\simeq 35$ mK at $z \simeq 40$. The subsequent rapid decrease in $f_{\mathrm{abs.}}$ once again results in the steady decrease of $\delta T_b - \delta T_{b,0}$, but the rate of decrease is sufficiently slow such that $\delta T_b - \delta T_{b,0} \simeq 9$ mK at $z = 10$, which should be comfortably detectable by interferometers such as LOFAR despite the various forms of foreground contamination (see § 8). However, as already discussed at the end of Sec. 5, this result holds if the Universe is still mostly neutral at this redshift. If this is not the case, we expect the signal associated to DM annihilations to rapidly go to zero as the Universe gets reionised.

8 DISCUSSION

We have calculated predictions for the effects on the evolution of the cosmological HI 21 cm signal during the Dark Ages for various forms of annihilating neutralino and light dark matter. Our calculations differ significantly compared to those conducted in previous studies since we include the enhancements in the annihilation rate arising from dark matter structures. We utilised results from the most recent

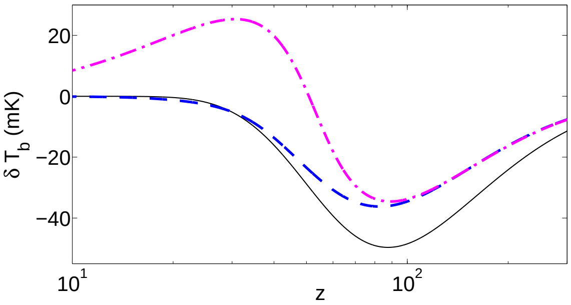

Figure 21. The 21 cm differential brightness temperature as a function of redshift. The black solid line displays the evolution of δT_b for the standard scenario where dark matter is absent, while the dashed lines correspond to δT_b for a Universe containing LDM particles of masses 3 MeV (blue dashed) and 20 MeV (magenta dot-dashed). Calculations were performed using the most optimistic clumping factors associated with structures possessing Burkert profiles that are consistent with the diffuse X-ray background, which in this instance were B7 and B12 for 3 MeV and 20 MeV LDM particles respectively.

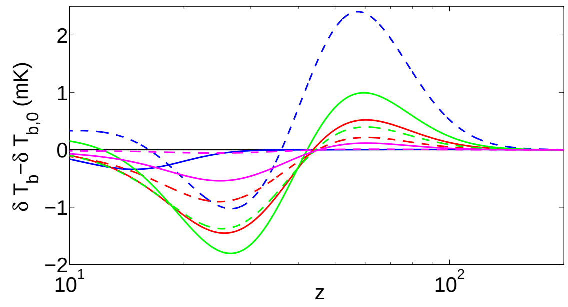

Figure 22. Difference in the 21 cm differential brightness temperature δT_b between that calculated for the standard case and that calculated using neutralino dark matter described by model 1 (blue), model 2 (red), model 3 (green) and model 4 (magenta). The results displayed correspond to those calculated using the most optimistic clumping factors for structures possessing Moore (solid) and NFW (dashed) profiles that were used to generate the results presented in § 7.

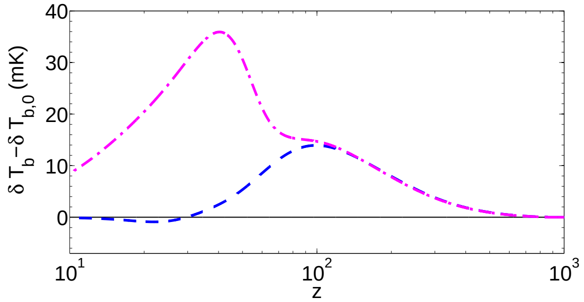

Figure 23. Difference in the 21 cm differential brightness temperature δT_b between that calculated for the standard case and that calculated for 3 MeV (blue dashed) and 20 MeV (magenta dot-dashed) LDM as displayed in figure 21.

state-the-art N-body simulations of dark matter halos to calculate the evolution of the enhancement in the annihilation rate, referred to as the “clumping factor”, owing to the distribution of halos and the self-similar distribution of increasingly smaller substructures predicted to exist within them, for a range of values of astrophysical parameters consistent with the uncertainties in the dynamics of the simulated halos. We performed detailed calculations of the absorbed fraction of the energy injected into the IGM by the annihilation products of our dark matter candidates. We used the standard equations for the evolution of the kinetic and spin temperatures of the IGM with modifications to account for the additional energy injected into, and subsequently absorbed, by the IGM from dark matter annihilations. Finally, we calculated the resulting deviations in the evolution of the differential brightness temperature δT_b, which is the quantity directly observed by radio interferometer experiments, relative to a scenario where dark matter is absent. If such deviations are sufficiently large, measurements by future radio telescopes, such as MWA, 21 CMA and SKA, may be sufficiently sensitive to discern and distinguish the effects of different species of dark matter.

Of particular interest are the impending LOFAR epoch of reionization experiments (LOFAR-EoR hereafter) designed to observe radio fluctuations at frequencies 115-215 MHz, corresponding to the redshifted 21 cm signal in the range $6 < z < 12$ (see e.g. Best (2008)). Unfortunately, the cosmological signal is contaminated by a plethora of astrophysical and non-astrophysical components - including, Galactic synchrotron emission from diffuse and localized sources (Shaver et al. 1999), Galactic free-free emission (Shaver et al. 1999), integrated emission from extragalactic sources, such as radio galaxies and clusters (Shaver et al. 1999; Di Matteo et al. 2002, 2004; Oh & Mack 2003; Cooray & Furlanetto 2004), ionospheric scintillation and instrumental response - the fluctuations of which can be up to three orders of magnitude greater than the cosmological signal (Jelić et al. 2008).

It is beyond the scope of this paper to provide a thorough treatment of the above forms of contamination, their modeling, and the methods employed to ultimately extract the cosmological signal. Many authors have studied these topics in detail (Shaver et al. 1999; Di Matteo et al. 2002; Zaldarriaga et al. 2004; Santos et al. 2005; Morales et al. 2006; Wang et al. 2006; Gleser et al. 2007; Jelić et al. 2008), and we refer the reader to such papers for further information. Here, we simply assume that such methods will be reliable enough so that LOFAR possesses a sensitivity in measurements of δT_b, after signal extraction, of order 1 mK for redshifts $z < 12$. [10] These estimates are based on preliminary results derived from simulations, conducted by LOFAR scientists, investigating the removal of foregrounds from the 21 cm background (Jelić et al. 2008).

We now apply the above sensitivity estimates to the results from our analysis. Firstly, we investigated dark matter composed of neutralinos, possessing masses ranging from 50-600 GeV, with being some Gaugino/Higgsino dominated, and an annihilation cross-section $\langle \sigma v \rangle \simeq 2.7 \times 10^{-26} \mathrm{cm}^3\mathrm{s}^{-1}$ which is consistent with current estimates for the currently-inferred abundance of dark matter in the Universe. Our results indicate that the evolution of the brightness temperature deviations $\delta T_b - \delta T_{b,0}$ for the widely varying forms of neutralino dark matter considered are similar to within a normalisation factor of order unity. Deviations of up to $\pm 2 - 3\,\mathrm{mK}$ are predicted to occur in the range $z = 50 - 70$ and $z = 20 - 30$. However, at frequencies detectable by LOFAR, such deviations are significantly reduced in all cases to less than $0.5\,\mathrm{mK}$ at $z \simeq 12$, placing them on the very edge of LOFARs detectability threshold, but certainly may be detectable by future experiments.

---

[10] We should mention however that the first luminous astrophysical objects in the Universe forming near to the epoch of reionisation, which from the most recent measurements by WMAP indicate could occur as early as $z = 14$ $(2\,\sigma)$ (Dunkley et al. 2008), could also produce a significant contribution to the global 21 cm signal.

We then investigated the effects of dark matter composed of annihilating LDM with masses of 3 and 20 MeV, with annihilation cross-sections of $\langle \sigma v \rangle \simeq 1.29 \times 10^{-29}$ and 8.60×10^{-29} $\mathrm{cm}^3\mathrm{s}^{-1}$, based on constraints derived from their predicted effects on the CMB. Our results predict significant deviation for 3 MeV LDM particles in the range $15 < z < 600$, rising to as much as $+15$ mK at $z \simeq 100$. However at later times, owing to the rapidly decreasing rate at which the IGM absorbs energy from the annihilation products of these particles, deviations in the brightness temperature are almost negligible at $z = 12$ and are unlikely to be detectable by LOFAR. However, for 20 MeV LDM the situation is far more optimistic with significant values of $\delta T_b - \delta T_{b,0}$ at all times $z < 800$, reaching 35mK at $z \simeq 50$, and approximately equal to $10\,\mathrm{mK}$ at $z = 12$, easily within the estimated sensitivity of LOFAR.

An interesting extension of our analysis would be to consider other dark matter particles, like exciting dark matter (XDM) (Finkbeiner & Weiner 2007). XDM can annihilate to produce two intermediate scalars ϕ that can subsequently decay to standard model particles. If $2m_e < m_\phi < 2m_\mu$, the ϕ will mainly decay to an e^+e^- pair, with an energy spectrum extending up to the mass of the XDM particle (Cholis, Goodenough & Weiner 2008).

Acknowledgements: DTC is supported by the Science and Technology Facilities Council. ML is supported by INFN. We would also like to thank Saleem Zaroubi for his very helpful discussions regarding LOFAR sensitivities.

REFERENCES

Akhmedov E. K., Berezhiani Z. G., Senjanovic G., 1992, Phys. Rev. Lett., 69, 3013

Allanach B. C., Dedes A., Dreiner H. K., 1999, Phys. Rev. D, 60, 075014

Asaka T., Shaposhnikov M., 2005, Phys. Lett. B, 620, 17

Asaka T., Blanchet S., Shaposhnikov M., 2005, Phys. Lett. B, 631, 151

Astier P. et al [The SNLS Collaboration], 2006, Astron. Astrophys., 447, 31

Avila-Reese V., Colín P., Valenzuela O., D'Onghia E., Firmani C., 2001, Astrophys. J., 559, 516

Bardeen J. M., Bond J. R., Kaiser N., Szalay A. S., 1986, Astrophys. J., 304, 15

Beacom J. F., Bell N. F., Bertone G., 2005, Phys. Rev. Lett., 94, 171301

Beacom J. F., Yuskel H., 2006, Phys. Rev. Lett., 97, 071102

Berezinsky V., Valle J. W. F., 1993, Phys. Lett. B, 318, 360

Bertone G., Hooper D., Silk J., 2005, Phys. Rept., 405, 279

Best P., 2008 arXiv:0802.1186 [LOFAR-UK Consortium]

Boehm C., Fayet P., 2004, Nucl. Phys. B, 683, 219

Boehm C., Schaeffer R., 2005, A&A, 438, 419

Boehm C., Uwer P., 2006, arXiv:hep-ph/0606058

Bullock J. S., Kolatt T. S., Sigad Y., Somerville R. S., Kravtsov A. V., Klypin A. A., Pimack J. R., Dekel A., 2001, MNRAS, 321, 559 (B2001)

Burkert A., 1995, Astrophys. J. Lett., 447,, L25

Chen X. L., Kamionkowski M, 2004, Phys. Rev. D, 70, 043502 [arXiv:astro-ph/0310473].

Cholis I., Goodenough L., Weiner N., 2008, preprint arXiv:0802.2922 [astro-ph]

Churazov E. et al., 2007, Astron. Astrophys., 467, 529

Chuzhoy L., 2007, arXiv:0710.1856 [astro-ph]

Ciardi B., Madau P., 2003, Astrophys. J., 596, 1

Cole S. et al. [The 2dFGRS Collaboration], 2005, Mon. Not. Roy. Astron. Soc., 362, 505

Colín P., Valenzuela O., Avila-Reese V., 2008, Astrophys. J., 673, 203

Cooray A., Furlanetto S. R., 2004, Astrophys. J., 606, L5

Dalcanton J. J., Hogan C. J., 2001, Astrophys. J., 561, 35

Diemand J., Kuhlen M., Madau P., Zemp M., Moore B., Potter D., Stadel J., 2008, arXiv:0805.1244

Di Matteo T., Perna R., Abel T., Rees M. J., 2002, Astrophys. J., 564, 576

Di Matteo T., Ciardi B., Miniati F., 2004, MNRAS, 355, 1053

Dodelson S, Widrow L. M., 1994, Phys. Rev. Lett. , 72, 17

Donato F., Gentile G., Salucci P., 2004, MNRAS, 353, L17

Dunkley J. et al. [WMAP Collaboration], 2008, arXiv:0803.0586 [astro-ph].

Field G. B., 1958, Proc, IRE, 46, 240

Field G. B., 1959, Astrophys. J., 129, 525

Finkbeiner D. P., Weiner N., 2007, Phys. Rev. D, 76, 083519

Flores R., Primack J. R., 1994, Astrophys. J. Lett., 427, L1

Furlanetto S. R., Oh S. P., Pierpaoli E., 2006, Phys. Rev. D, 74, 103502

Gentile G., Salucci P., Klein U., Granato G. L. 2007, MNRAS, 375, 199

Gleser L., Nüsser A., Benson A. J., 2007,arXiv:0712.0497 [astro-ph]

Hall L. J., Suzuki M., 1984, Nucl. Phys. B, 231, 419

Hirata C. M., 2006, MNRAS, 367, 259

Hogan C. J., Dalcanton J. J., 2000, Phys. Rev. D, 62, 063511

Hooper D., Taylor J. E., Silk J., 2004, Phys. Rev. D, 69, 103509

Jelić V. et al, 2008, arXiv:0804.1130 [astro-ph]

Jenkins A. et al., 1998, Astrophys. J., 499, 20

Knebe A., Arnold B., Power C., Gibson B. K., 2008, MNRAS, 386, 1029

Knödlseder J. et al., 2005, A&A, 441, 513

Komatsu E. et al. [WMAP Collaboration], arXiv:0803.0547 [astro-ph].

Kuhlen M., Madau P., Montgomery R., 2006, Astrophys. J., 637, L1-L4
Kuhlen M., Diemand J., Madau P., 2008 (arXiv:0805.4416) (KDM)
Lattanzi M., Valle J. W. F., 2007, Phys. Rev. Lett. 99, 121301
Liszt H., 2001 A&A, 371, 698
Moore B., 1994, Nature (London), 370, 629
Moore B., Quinn T., Governato F., Stadel J., Lake G., 1999, MNRAS, 310, 1147
Morales M. F., Bowman J. D., Hewitt J. N., 2006, Astrophys. J., 648, 767
Navarro J. F., Frenk C. S., White S. D. M., 1996, Astrophys. J., 462, 563
Navarro J. F., Frenk C. S., White S. D. M., 1997, Astrophys. J., 490, 493
Oh S. P., Mack K. J., 2003, MNRAS, 346, 871
Padmanabhan N., Finkbeiner D. P., 2005, Phys. Rev. D, 72, 023508
Pengelly R. M., 1964 MNRAS, 127, 145
Press W., Schechter E., 1974, Astrophys. J., 187, 425
Profumo S., Sigurdson K., Kamionkowski M., 2006, Phys. Rev. Lett., 97, 031301
Ripamonti E., Mapelli M. and Ferrara A., 2007, Mon. Not. Roy. Astron. Soc. , 374, 1067
Salucci P., Burkert A., 2000, Astrophys. J. Lett., 537, L9
Santos M. G., Cooray A., Knox L., 2005, Astrophys. J., 625, 575
Seager S., Sasselov D. D., Scott D., 1999, Astrophys. J., 523, 1
Seager S., Sasselov D. D., Scott D., 2000, ApJ Suppl., 128, 407-430
Shaver P. A., Windhorst R. A., Madau P., de Bruyn A. G., 1999, A&A, 345, 380
Shchekinov Y. A., Vasiliev E. O., 2007, Mon. Not. Roy. Astron. Soc. , 379, 1003
Sheth R., Tormen G., 2002, MNRAS, 329, 61
Shull J. M., van Steenberg M. E., 1985, Astrophys. J., 298, 268
Sjostrand T., Eden P., Friberg C., Lonnblad L., Miu G., Mrenna S., Norrbin E., 2001, Comput. Phys. Commun., 135, 238
Smith H., 1966 P&SS, 14, 929
Spergel D. N. et al. [WMAP Collaboration], Astrophys. J. Suppl. , 148, 175 (2003)
Spergel D. N. et al. [WMAP Collaboration], Astrophys. J. Suppl. , 170, 377 (2007)
Sreekumar P. et al. [EGRET Collaboration], 1998, Astrophys. J., 494, 52
Strong A. W., Moskalenko I. V., Reimer O., 2004, Astrophys. J., 613, 956
Taylor J. E., Silk J., 2003, MNRAS, 339, 505
Tegmark M., Vilenkin A., Pogosian L., 2005, Phys. Rev. D, 71, 103523
Tegmark M., Aguirre A., Rees M., Wilczek F., 2006, Phys. Rev. D, 73, 023505
Tegmark M. et al. [SDSS Collaboration], 2006, Phys. Rev. D, 74, 123507
Ullio P., Bergström L., Edsjö J., Lacey C., 2002, Phys. Rev. D, 66, 123502
Valdés M., Ferrara A., Mapelli M., Ripamonti E., 2007, MNRAS, 377, 245
Weidenspointner G. et al., 2000, AIP Conf. Proc. 510, 467.
Wood-Vasey W. M. et al., [ESSENCE Collaboration], 2007, Astrophys. J. , 666, 694
Wouthuysen S. A., 1952, AJ, 447, 31
Wang X., Tegmark M., Santos M. G., Knox L., 2006, Astrophys. J., 650, 529
Weinberg S., 1982, Phys. Rev. D, 26, 287
Weldrake D. T. F., de Blok W. J. G., Walter F., 2003, MNRAS, 340, 12
Zaldarriaga M., Furlanetto S. R., Hernquist L., 2004, Astrophys. J., 608, 622
Zdziarski A. A., Svensson R., 1989, Astrophys. J., 344, 551

APPENDIX

In this section we conveniently list the relevant parameters associated with each of the clumping factors utilised throughout this study, for clumping factors calculated using structures possessing Moore (table 1) and NFW (table 2) profiles for our four neutralino dark matter models, and for Burkert profiles using our two LDM candidates (table 3).

	$n_{\mathrm{min.}}$	n_{cut}	$F_{\mathrm{sub.}}, F_{ss}$ (%)	N_c	Model 1	Model 2	Model 3	Model 4
M1	-12	-12	3	3	N	N	N	N
M2	-12	-12	3	1.5	N	N	N	N
M3	-12	-12	0.3	3	N	N	N	N
M4	-12	-12	0.3	1.5	N	N	N	Y, (-0.12)
M5	-12	6	3	3	N	N	N	N
M6	-12	6	3	1.5	N	N	N	Y, (-0.04)
M7	-12	6	0.3	3	N	N	Y, (0.02)	Y, (-0.04)
M8	-12	6	0.3	1.5	N	Y, (-0.23)	Y, (-0.08)	Y, (-0.04)
M9	-4	-4	3	3	N	N	N	N
M10	-4	-4	3	1.5	N	N	N	N
M11	-4	-4	0.3	3	N	N	N	Y, (-0.07)
M12	-4	-4	0.3	1.5	N	N	N	Y, (-0.06)
M13	-4	6	3	3	N	N	Y, (0.15)	N
M14	-4	6	3	1.5	N	N	Y, (-0.21)	Y, (-0.03)
M15	-4	6	0.3	3	N	N	Y, (-0.21)	Y, (-0.03)
M16	-4	6	0.3	3	N	Y, (-0.23)	Y, (-0.09)	Y, (-0.03)
M17	6	6	3	3	N	Y, (-0.05)	Y, (-0.09)	Y, (0.00)
M18	6	6	3	1.5	Y, (-0.27)	Y, (-0.05)	Y, (-0.09)	Y, (0.00)
M19	6	6	0.3	3	Y, (-0.27)	Y, (-0.05)	Y, (-0.09)	Y, (0.00)
M20	6	6	0.3	1.5	Y, (-0.27)	Y, (-0.05)	Y, (-0.09)	Y, (0.00)

Table 1. Parameters for the clumping factors used to generate the results presented for structures possessing Moore density profiles. For each clumping factor, the following parameters are displayed in each column (from left to right): column (1) - indicates the clumping factor designation; column (2) - $n_{\mathrm{min.}} = \log_{10}(M_{\mathrm{min.}}/M_\odot)$, where $M_{\mathrm{min.}}$ is the minimum halo mass considered; column (3) - $n_{\mathrm{cut.}} = \log_{10}(M_{\mathrm{cut.}}/M_\odot)$, where $M_{\mathrm{cut.}}$ is the mass below which the concentration-mass relation for halos is truncated; column (4) - percentage of host halo (subhalo) mass per mass decade in subhalos (sub-subhalos), column (5) - ratio of concentrations for a subhalo and halo of the same mass located at the same redshift; column (6) - indicates whether the relevant clumping factor satisfies the criterion discussed in § 7 regarding constraints on the diffuse background ('N' for No, 'Y' for Yes) for neutralino dark matter described by model 1; Column (7) (also under the heading 'model 1') - indicates the value of the differential brightness temperature difference relative to the standard "no dark matter" scenario, $\delta T_b - \delta T_{b,0}$ (mK), evaluated at redshift $z = 12$ (provided that column (5) is 'Y') for neutralino dark matter described by model 1; Columns (8)&(9) are the same as for columns (6)&(7) but for neutralino dark matter described by model 2; Columns (10)&(11) are the same as for columns (6)&(7) but for neutralino dark matter described by model 3; Columns (12)&(13) are the same as for columns (6)&(7) but for neutralino dark matter described by model 4.

	$n_{\mathrm{min.}}$	n_{cut}	$F_{\mathrm{sub.}}, F_{ss}$ (%)	N_c	Model 1	Model 2	Model 3	Model 4
N1	-12	-12	3	3	N	N	N	N
N2	-12	-12	3	1.5	N	Y, (-0.21)	Y, (-0.24)	Y, (-0.02)
N3	-12	-12	0.3	3	N	Y, (-0.18)	Y, (-0.23)	Y, (-0.02)
N4	-12	-12	0.3	1.5	Y, (0.31)	Y, (-0.13)	Y, (-0.20)	Y (-0.01)
N5	-12	6	3	3	N	N	Y, (-0.24)	Y, (-0.02)
N6	-12	6	3	1.5	Y, (-0.23)	Y, (-0.05)	Y, (-0.08)	Y (0.00)
N7	-12	6	0.3	3	Y, (-0.23)	Y, (-0.05)	Y (-0.08)	Y (0.00)
N8	-12	6	0.3	1.5	Y, (-0.22)	Y (-0.04)	Y (-0.07)	Y (0.00)
N9	-4	-4	3	3	N	N	N	Y (-0.02)
N10	-4	-4	3	1.5	Y, (-0.15)	Y, (-0.09)	Y, (-0.14)	Y, (-0.01)
N11	-4	-4	0.3	3	Y, (-0.17)	Y, (-0.08)	Y, (-0.13)	Y (-0.01)
N12	-4	-4	0.3	1.5	Y, (-0.20)	Y, (-0.07)	Y, (-0.11)	Y (-0.01)
N13	-4	6	3	3	N	Y, (-0.07)	Y (-0.11)	Y, (-0.11)
N14	-4	6	3	1.5	Y, (-0.21)	Y, (-0.04)	Y (-0.06)	Y (0.00)
N15	-4	6	0.3	3	Y, (-0.21)	Y, (-0.04)	Y (-0.06)	Y (0.00)
N16	-4	6	0.3	3	Y, (-0.20)	Y (-0.03)	Y (-0.06)	Y (0.00)
N17	6	6	3	3	Y, (-0.04)	Y (0.00)	Y (-0.01)	Y (0.00)
N18	6	6	3	1.5	Y (-0.04)	Y (0.00)	Y (-0.01)	Y (0.00)
N19	6	6	0.3	3	Y (-0.04)	Y (0.00)	Y (-0.01)	Y (0.00)
N20	6	6	0.3	1.5	Y (-0.04)	Y (0.00)	Y (-0.01)	Y (0.00)

Table 2. Same as for table 1 but for clumping factors associated with structures possessing NFW density profiles.

	$n_{\rm min.}$	$n_{\rm cut}$	$F_{\rm sub.}, F_{ss}$ (%)	N_c	$m_{\rm LDM} = 20\,{\rm MeV}$	$m_{\rm LDM} = 3\,{\rm MeV}$
B1	-0.80	-0.80	3	3	N	-
B2	-0.80	-0.80	3	1.5	N	-
B3	-0.80	-0.80	0.3	3	N	-
B4	-0.80	-0.80	0.3	1.5	N	-
B5	-0.80	6	3	3	N	-
B6	-0.80	6	3	1.5	N	-
B7	-0.80	6	0.3	3	Y, (11.03)	-
B8	-0.80	6	0.3	1.5	Y, (10.70)	-
B9	1.66	1.66	3	3	-	N
B10	1.66	1.66	3	1.5	-	N
B11	1.66	1.66	0.3	3	-	N
B12	1.66	1.66	0.3	1.5	-	Y, (-0.18)
B13	1.66	6	3	3	-	N
B14	1.66	6	3	1.5	-	N
B15	1.66	6	0.3	3	-	Y, (-0.15)
B16	1.66	6	0.3	1.5	-	Y, (-0.15)
B17	6	6	3	3	Y, (2.07)	N
B18	6	6	3	1.5	Y, (2.04)	Y, (-0.15)
B19	6	6	0.3	3	Y, (1.90)	Y, (-0.04)
B20	6	6	0.3	1.5	Y, (1.90)	Y, (-0.04)

Table 3. Same as for table 1 but for clumping factors associated with structures possessing Burkert density profiles and using LDM of mass 20 MeV (columns (6)&(7)) and 3 MeV (columns (8)&(9)).